

# CCFM Evolution with Unitarity Corrections

Emil Avsar, Edmond Iancu

*Institut de Physique Théorique de Saclay, F-91191 Gif-sur-Yvette, France*

---

## Abstract

We considerably extend our previous analysis of the implementation of an absorptive boundary condition, which mimics saturation effects, on the linear CCFM evolution. We present detailed results for the evolution of the unintegrated gluon density in the presence of saturation and extract the energy dependence of the emerging saturation momentum. We show that CCFM and BFKL evolution lead to almost identical predictions after including the effects of gluon saturation and of the running of the coupling. We moreover elucidate several important and subtle aspects of the CCFM formalism, such as its relation to BFKL, the structure of the angular ordered cascade, and the derivation of more inclusive versions of CCFM. We also propose non-leading modifications of the standard CCFM evolution which may play an important role for phenomenological studies.

---

## 1. Introduction

In a previous work, Ref. [1], we have proposed a method for effectively implementing saturation and unitarity within a generic linear evolution equation for the unintegrated gluon distribution, so like the BFKL [2] and the CCFM [3, 4, 5] equations. The method is based on enforcing an absorptive boundary condition at low transverse momenta which prevents the gluon phase-space occupation numbers to grow beyond their physical values at saturation. Our method is the extension of a strategy originally introduced in relation with analytic studies of the BFKL evolution in the presence of saturation [6, 7], whose deeper justification [8] lies in the correspondence between high-energy evolution in QCD and the reaction-diffusion process in statistical physics [9]. This correspondence is however limited to asymptotically high energies and to a fixed coupling [10], whereas our analysis in Ref. [1] shows that the absorptive boundary method is in fact more general and also very powerful. After reformulating this method in such a way to be suitable for numerical simulations, we have demonstrated its efficiency by comparing the numerical solutions to the BFKL equation with absorptive boundary condition against those of the proper non-linear generalization of BFKL which includes saturation — the Balitsky-Kovchegov (BK) equation [11, 12]. We have thus shown that the absorptive boundary method successfully reproduces the results of the BK equation for both fixed and running coupling, and for *all* the energies, and not only the asymptotic ones. This success, together with its relative

---

*Email addresses:* [Emil.Avsar@cea.fr](mailto:Emil.Avsar@cea.fr), [Edmond.Iancu@cea.fr](mailto:Edmond.Iancu@cea.fr) (Emil Avsar, Edmond Iancu)

simplicity, makes this method a very compelling tool for phenomenological studies at LHC and, in particular, for implementing saturation within Monte Carlo based event generators, such as CASCADE [13] and LDCMC [14]. Most importantly, our effective method can be also implemented within formalisms whose non-linear generalizations are not known, so like the CCFM formalism [3, 4, 5] which lies at the basis of the above mentioned generators. It is our main purpose in this paper to provide an extensive numerical study of the CCFM evolution supplemented with the absorptive boundary condition, and thus demonstrate the role of the saturation effects in that context. Some preliminary results in that sense were already presented in Ref. [1], but our present analysis will considerably enlarge that previous analysis, in particular by exploring the CCFM formalism in much more detail.

Based on our current theoretical understanding and on extrapolations from the phenomenology at HERA and RHIC, we expect at LHC a considerably larger phase space where saturation effects should be important. The characteristic transverse momentum scale for the onset of unitarity corrections is the saturation momentum  $Q_s$ , and is expected to grow quite fast with increasing energy. Next-to-leading order BFKL calculations [15] suggest a power law  $Q_s^2 \sim s^\lambda$  with  $\lambda \simeq 0.2 \div 0.3$ , which appears to be supported by the HERA data at small  $x \leq 0.01$  [16, 17, 18]. For forward jet production in proton-proton collisions at LHC, one thus expects  $Q_s$  in the ballpark of 2 to 3 GeV. Even higher values could be reached in nucleus-nucleus collisions, or in some rare events, like Mueller-Navelet jets [19].

*A priori*, it seems natural to look for saturation effects in the underlying event, that is, in the bulk of the particle production at relatively low momenta, where the saturation effects (also viewed as multiple scattering [20, 21]) are clearly important. However, the underlying event at LHC will be extremely complex and difficult to study. Besides, for such low momenta, it may be difficult to separate saturation physics from the genuinely non-perturbative physics in the soft sector of QCD. (A similar ambiguity occurs in the interpretation of the small- $x$  data at HERA.) It is therefore useful to recall at this point that saturation effects can make themselves felt even at relatively large momenta  $Q$ , well above  $Q_s$ , via phenomena like the “geometric scaling” observed at HERA [16, 22, 23]. Such phenomena, which reflect the change in the unintegrated gluon distribution at high  $k_\perp \gg Q_s$  due to saturation at low  $k_\perp \lesssim Q_s$  [6, 7, 15, 8], are particularly interesting in that they represent signatures of saturation in the high- $Q^2$  domain which was traditionally believed to fully lie within the realm of the “standard” pQCD formalism — the DGLAP evolution [24] of the parton distributions together with the collinear factorization of the hadronic cross-sections.

Schemes based on the NLO DGLAP evolution have been quite successful at HERA (at least for not too low  $Q^2$ ) [25], but at LHC one will probe much smaller values of Bjorken  $x$ , and this even for relatively hard  $Q^2$  (e.g., in the forward kinematics). The jets to be measured at LHC will carry relatively large transverse momenta  $Q \geq 10$  GeV, but because of the high-energy kinematics, their description may require  $k_\perp$ -factorization [26] together with the BFKL, or CCFM, evolution of the unintegrated gluon distribution. Moreover, saturation effects, like geometric scaling, could manifest themselves in hard observables at LHC, so like the cross-section for forward jet production [19]. Thus LHC will for the first

time allow us to study saturation physics in the kinematical regime where this physics lies in the realm of perturbative QCD.

The BFKL formalism, properly generalized to include the non-linear effects responsible for gluon saturation [11, 12, 27, 28, 29], is specially tailored to describe the evolution of the unintegrated gluon distribution with increasing energy and its approach towards saturation. As such, this is well-suited to study the high-energy evolution of inclusive cross-sections, and it is able to accommodate important phenomena, like the geometric scaling at HERA [16, 22, 23], or the turnover in the DIS structure function  $F_2(x, Q^2)$  at semi-hard  $Q^2$  [17, 18]. However, this is not the right formalism to also describe exclusive final states, because it misses the quantum coherence between successive gluon emissions in the process of high-energy evolution. Besides, there are additional problems, to be discussed at the end of section 2.3, which make the BFKL formalism unsuitable for studying exclusive final states. All such problems are corrected in the CCFM formalism [3, 4, 5], which has also the advantage to apply within a wider kinematical region, interpolating between the high energy evolution (the realm of BFKL) and the evolution with increasing virtuality (the realm of DGLAP). A similar formalism derived out of CCFM but using a different physical picture for the evolution is the Linked Dipole Chain (LDC) model [30] which covers the same kinematical region as CCFM, and our method of implementing saturation can be equally well applied also to this formalism. Infact one of the main equations to which we apply our method is equivalent to the master equation in LDC. This will be discussed more below.

Like BFKL, the CCFM formalism is based on the  $k_\perp$ -factorization. This makes it possible to take into account some of the NLO corrections in the collinear approach by simply treating the kinematics of the scattering more accurately [31, 32, 33]. Still like BFKL, the CCFM evolution resums all powers of  $\alpha_s$  which are accompanied by large energy logarithms  $\ln s$ , with  $s$  the center of mass energy. In fact, the CCFM and BFKL evolutions yield identical predictions for the dominant behaviour in the formal high-energy limit  $s \rightarrow \infty$ . But this formal limit is conceptually unrealistic and phenomenologically irrelevant, since it violates unitarity. What is relevant, is the approach towards the unitarity limit and gluon saturation with increasing energy, which is *a priori* different in the two formalisms. In the recent years, this approach has been extensively studied within the BFKL evolution, by using its non-linear generalizations: the BK [11, 12] and the JIMWLK equations [27, 28]. However, no such a study was performed within the context of the CCFM evolution prior to our recent work [1]. As already stated, such a study is the main objective of the present work.

The present study should be viewed as a step towards a systematic inclusion of the effects of saturation in the description of exclusive final states. Most studies have so far concentrated on more inclusive observables, for which a good description can generally be obtained (for sufficiently high  $Q^2$ ) also with linear evolution equations alone. A number of papers emphasized the need and importance of studying saturation in exclusive final states [34, 35, 36, 37], but so far the explicit studies were mostly confined to inclusive observables. The possibility of looking at more exclusive observables will undoubtedly make it easier to distinguish the predictions of linear and non-linear evolutions.

But before we consider the effects of saturation, we shall dedicate a large part of this

paper to a detailed presentation of the respective linear evolution, in order to clarify several non-trivial aspects of the CCFM formalism which are important for our purposes. In doing so, we will try to carefully motivate the steps leading to the final evolution equations (simplified versions of the CCFM formalism) on which we shall apply our saturation boundary. Among the different aspects of CCFM to be discussed here, there are parts which have been already presented in previous papers that we shall refer to, but there are also parts which to our knowledge have never been presented before. In this paper, we shall try to give a unified presentation of all the relevant aspects, using an intuitive geometrical representation for the phase-space of the CCFM evolution. To facilitate the reading of the paper, we have moved some of the most technical developments to appendices, and kept only the important results in the main text. Here is a summary of the topics to be covered in what follows and also of our main conclusions:

Sect. 2 will introduce the basics of the CCFM formalism, that the rest of the work will rely on. In particular, in Sect. 2.2 we shall clarify the relation between the phase-space of the CCFM evolution and that of the BFKL evolution, thus recovering previous results in Ref. [38], but from a different perspective. In Sect. 2.3 we shall present the standard version of the CCFM evolution as an integral equation, and on this occasion we shall explain the approximations which are involved in this rewriting and which are often kept implicit in the literature. In Sect. 2.4 and Appendix A we discuss some subtle aspects, and correct some mistakes in the literature, concerning the virtual (‘non-Sudakov’) form factors which express the probability for not emitting gluon in the course of the evolution. The careful derivation of these form factors, as outlined in Sects 2.3 and 2.4 and in Appendix A, will also allow us to better understand their physical origin and thus propose some improved expressions for them, which treat more accurately the kinematics (by including effects of recoils in the energy). The new form factors, to be presented in appendix B, differ from the standard ones by terms which are formally of higher order, but which may be numerically important<sup>1</sup> and thus interesting for the phenomenology. Another aspect of the form factor is its appropriate form in the formal high energy limit, which is relevant again for the comparison to BFKL and this will be discussed in appendix C.

Sections 3 and 4 are the key sections in this paper. In Sect 3 we successively simplify the CCFM formalism and reduce it to a set of simpler, integral and differential, equations, which are more suitable for numerical simulations. The most general equation, the integral equation (3.1), explicitly preserves all the hard and soft gluon emissions from the  $t$ -channel propagators. This is the equation at the basis of the CASCADE Monte Carlo event generator [13], and it can be generalized to include saturation effects, as we shall explain in Sect. 4.1. But for the present purposes, it is preferable to work with simpler versions of the CCFM evolution, namely Eqs. (3.11) and (3.12), which are more ‘inclusive’ — in the sense that some of the virtual form factors are used to cancel the ‘soft’ gluon emissions. Such cancellations are not exact, but rather require some additional kinematical approximations, which are however in the spirit of the CCFM formalism. These approximations are also

---

<sup>1</sup>We shall not include these new form factors in our present numerical analysis since their structure is such that they can be efficiently implemented only within Monte Carlo simulations.

similar to those underlying the ‘Linked Dipole Chain’ (LDC) model [30]. And indeed, our Eq. (3.11) appears to be equivalent to the master equation in Ref. [30], although our respective approaches are quite different. Intriguingly, it turns out that if one performs the same type of approximations starting with the BFKL formalism, one is again led to the same two equations (3.11) and (3.12) (see the discussion in Sect. 3.4). In our opinion, this points out towards a deep similarity between the BFKL and CCFM formalisms, which when applied to inclusive observables differ only in the accuracy to which they treat the kinematics.

In Sect. 4 we introduce the absorptive boundary method which effectively implements saturation within a linear evolution equation, so like BFKL or CCFM. First, in Sect. 4.1, we describe this method on the example of the BFKL equation, where the comparison with the non-linear BK equation will allow us to demonstrate the success of the method. Then, in Sect. 4.2, we analytically study the high-energy behaviour of the approximate CCFM equations (3.11) and (3.12) and thus determine the energy-dependence of the associated saturation momenta, in the case of a fixed coupling. Our analysis shows that the CCFM evolution is somewhat faster than the BFKL one: the respective saturation exponent is slightly larger. On the other hand, the characteristic functions which determine the momentum-dependent anomalous dimension, are very similar to the BFKL one, for both Eq. (3.11) and Eq. (3.12). In Appendix D, we relax some of the approximations used in deriving Eq. (3.11) and thus obtain a more accurate equation, whose high-energy predictions are even closer to those of the BFKL equation.

Finally, Section 5 presents a systematic numerical analysis of the various evolution equations — the BFKL equation and the simplified versions, Eqs. (3.11) and (3.12), of the CCFM evolution — with the purpose to illustrate the role of the saturation boundary and also of the running coupling effects. We first demonstrate that the respective linear equations (no saturation boundary) lead to rather different evolutions, which are moreover infrared unstable in the case of a running coupling. Then we show that the infrared instability is cured after including the saturation boundary (the saturation momentum effectively acts as a hard infrared cutoff which increases with the energy) and moreover the respective predictions of the various equations remain very close to each other, up to astronomically high energies. Hence, in so far as the unintegrated gluon distribution is concerned, the BFKL and CCFM evolutions properly corrected for saturation and endowed with a running coupling are rather similar to each other.

## 2. Review of CCFM

Our aim in this section is to review the CCFM approach, mainly the work in [4]. This will prepare us in understanding our subsequent strategy for simplifying this formalism and most efficiently complete it with a saturation boundary. The original formulation in [4] is very careful and complete, but also quite technical and not always transparent. We shall therefore try to mostly give a geometrical representation of the equations to be presented here. In this process, we will derive to some interesting results that we were not aware of, and also clarify some points which are often confusing in the literature, such as the precise form of the “non-Sudakov” form factor  $\Delta_{ns}$ .

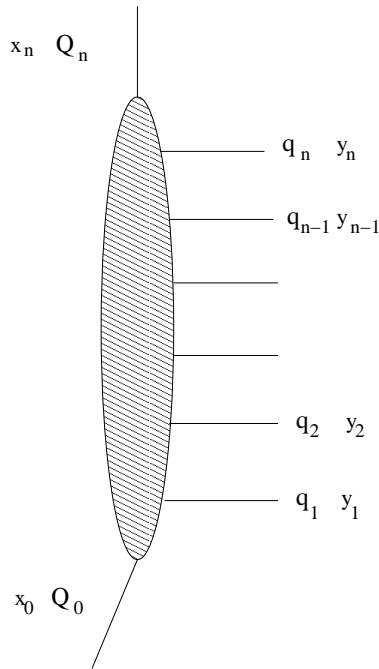


Figure 1: *Kinematics of the gluon radiation.* The last  $t$ -channel propagator is denoted by  $Q_n$ , while the real  $s$ -channel gluons are represented by the horizontal lines.

### 2.1. Kinematics and Basics

We use Fig. 1 to define the kinematics and schematically introduce the physical picture. This figure represents a gluon ladder as produced by the CCFM evolution; we denote by  $q_i$  the transverse momenta of the real,  $s$ -channel, gluons, and with  $Q_i$  the transverse momenta of the space-like,  $t$ -channel, propagators, which are not explicitly shown in the figure. The incoming virtual gluon has zero transverse momentum  $Q_0 = 0$  (that is, this gluon is taken to be collinear with the parent hadron, not shown here), and hence one has  $Q_i = -\sum_{k=1}^i q_k$ . We will use  $y_i$  and  $x_i$  to denote the energy fractions of the  $s$ -channel and  $t$ -channel gluons, respectively, measured with respect to the energy  $E$  of the incoming proton. In Fig. 1, the  $s$ -channel (or ‘real’) gluons are enumerated according to their energy:

$$x = x_n \ll y_n \ll y_{n-1} \ll \cdots \ll y_2 \ll y_1 \approx 1, \quad (2.1)$$

but this ordering is not necessarily the same as that of the gluon emissions along the ladder (i.e., it is not assumed that the gluon with energy fraction  $y_i$  is emitted out right after that with fraction  $y_{i-1}$ , etc.). Rather, as we shall shortly see, the real gluon emissions in the CCFM ladder are ordered according to their angles  $\xi_i \equiv q_i^2/(y_i^2 E^2)$ . This ordering issue is potentially confusing, since e.g. the relation  $Q_i = -\sum_k^i q_k$  would be strictly true if the labels  $i$  attached to gluons in Fig. 1 were also indicating their order of emission, i.e., if the real gluons emissions were ordered according to their energy (which they are not). The resolution of this puzzle, to be explained in detail later on, is that the actual

emissions which do not obey energy ordering are also soft in the sense of carrying little transverse momenta ( $k_{\perp}$ -conserving'), and hence they do not affect the momenta  $Q_i$  of the  $t$ -channel gluons: the latter are fully determined by the 'hard' emissions which are simultaneously ordered in angle and in energy. (See Sect. 2.3 for details.)

The (integrated) CCFM gluon structure function can be written as

$$\mathcal{A}(x, \bar{\xi}) = \sum_n \int \prod_{i=1}^n \left( \bar{\alpha}_s \frac{d\xi_i}{\xi_i} \theta(\bar{\xi} - \xi_i) \frac{dy_i}{y_i} \theta(y_i - y_{i+1}) \sum_{perm} \theta(\xi_{l_i} - \xi_{l_{i-1}}) \right) \times \frac{1}{x_n} \delta(x - x_n) S_{eik}^2(y_1, \bar{\xi}) S_{ne}^2(12 \dots n) \quad (2.2)$$

where  $y_{n+1} \equiv 0$ , and  $S_{eik}$  and  $S_{ne}$  are the virtual corrections associated with the eikonal and the non-eikonal vertices respectively. The theta function  $\theta(\xi_{l_i} - \xi_{l_{i-1}})$  is a consequence of the quantum coherence between successive emission which implies that the emission angle must increase when moving upwards along the ladder (*i.e.*, towards the hard scattering). Notice that one can have any angular ordering for the given energy ordering. (We shall later relabel the real gluons according to the angular ordering.) The angle  $\bar{\xi}$  in the argument of  $\mathcal{A}$  is the maximum angle allowed by coherence and is determined by the kinematics of the hard scattering; roughly,  $\bar{\xi} \simeq Q^2/x^2 E^2$  with  $Q^2$  the virtuality of the incoming photon. In this case, the structure function (2.2) gives the gluon distribution,  $\mathcal{A}(x, \bar{\xi}) = xg(x, Q^2)$  [39].

The virtual form factors in (2.2) are given by

$$S_{eik}(y_1, \bar{\xi}) = \exp \left( -\frac{1}{2} \bar{\alpha}_s \int^{y_1} \frac{dy}{y} \int^{\bar{\xi}} \frac{d\xi}{\xi} \right) \quad (2.3)$$

$$S_{ne}(12 \dots n) = \prod_{k=1}^n \exp \left( \frac{1}{2} \bar{\alpha}_s \int_{y_{k+1}}^{y_k} \frac{dy}{y} \int_{\xi(Q_k)}^{\bar{\xi}} \frac{d\xi}{\xi} \right) \equiv \prod_{k=1}^n S_{ne}(k) \quad (2.4)$$

where  $\xi(Q_k) \equiv Q_k^2/(y^2 E^2)$  and the integral over the transverse momentum  $q^2$  has been written in terms of the associated angular variable  $\xi^2 \equiv q^2/y^2 E^2$ . Notice that the exponent in the non-eikonal form factor is positive. The apparent divergence in  $S_{eik}$  and in the real emission density  $d\xi/\xi$  is regulated by a collinear momentum cut  $q_0$  (which also regulates the  $dy/y$  divergence in  $S_{eik}$ ).

One should be aware that (2.2) does not correspond to an exclusive final state. In (2.2) one has already inclusively summed over all subsequent emissions from the outgoing gluons  $q_i$ . Each such gluon can further radiate within a cone of half opening angle  $\xi_i$ . These final emissions are such that the real emission probability is exactly compensated by virtual corrections of the type  $S_{eik}$ , and they are therefore not visible in the expression (2.2) for the (inclusive) gluon distribution. For the study of exclusive final states, however, one needs to include all the emissions.

## 2.2. The phase space and relation to BFKL

In this subsection we shall describe in detail the phase-space for real and virtual gluon emissions within the CCFM ladder and then argue that, up to subleading effects, this is

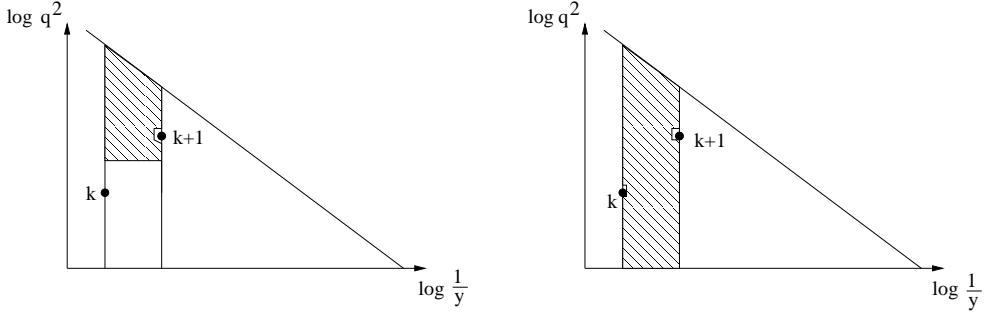


Figure 2: Geometrical representation of two emissions (fat dots) in CCFM shown in the  $(\ln(1/y), \ln q^2)$ -phase space. The total phase space is bounded by the diagonal line which indicates the maximal angle allowed by coherence. The shaded regions show the phase regions over which  $S_{ne}(k)$  (left) and  $S_{eik}$  (right) are integrated over.

essentially the same as the phase-space for the BFKL evolution. This will allow us to conclude that the CCFM and BFKL evolutions become identical with each other in the high energy limit. (See also Ref. [38] for similar considerations.)

Let us start with the virtual emissions and rewrite the eikonal form factor in (2.3) as

$$\begin{aligned}
 S_{eik}(y_1, \bar{\xi}) &= \prod_{k=1}^n \exp \left( -\frac{1}{2} \bar{\alpha}_s \int_{y_{k+1}}^{y_k} \frac{dy}{y} \int^{\bar{\xi}} \frac{d\xi}{\xi} \right) \\
 &\equiv \prod_{k=1}^n S_{eik}(k)
 \end{aligned} \tag{2.5}$$

with  $y_{n+1} \equiv 0$ . Let us now consider the two emissions in Fig. 2. In this figure the horizontal axis<sup>2</sup> is  $\ln(1/y)$  while the vertical axis is  $\ln(q/q_0^2)$  (from now on we shall for simplicity omit using  $q_0$ ). A black dot in such figures denotes a real gluon with the respective values for the energy ( $y$ ) and the transverse momentum ( $q^2$ ). Since  $\ln \xi = \ln(q^2/y^2 E^2) = \ln(q^2/E^2) + 2 \ln(1/y)$ , the emission angle will be constant along diagonal lines in the figure. The diagonal line shown in figure 2 denotes the maximum angle, determined by  $\bar{\xi}$ . The diagonal lines parallel to this line and which pass through the gluons will indicate the angle of the gluons (see e.g. Fig. 5).

The shaded regions in the two figures indicate the phase space over which the non-eikonal and eikonal form factors are integrated over. The rightmost figure, representing  $S_{eik}(k)$ , is easier to understand. Here the  $y$  integral is bounded by  $y_{k+1}$  and  $y_k$ , that is we integrate over the region between the two vertical lines, and the  $\xi$  integral goes up to  $\bar{\xi}$ , as can be seen in the figure. To understand the leftmost figure, note that in  $S_{ne}(k)$  defined in (2.4), the  $y$ -integral is the same as in  $S_{eik}(k)$  while the  $\xi$ -integral (or, equivalently, that over  $q^2 = y^2 E^2 \xi^2$ ) is integrated from  $Q_k^2$  up. The horizontal line bounding the shaded region in that figure corresponds to  $\ln Q_k^2$ . Since the exponent is negative in  $S_{eik}(k)$  and is

<sup>2</sup>These type of diagrams have been widely used for example in [30], but notice that there the horizontal is taken as  $\ln(\xi)$  instead of  $\ln(1/y)$ . Our choice is the same as the one in [38].



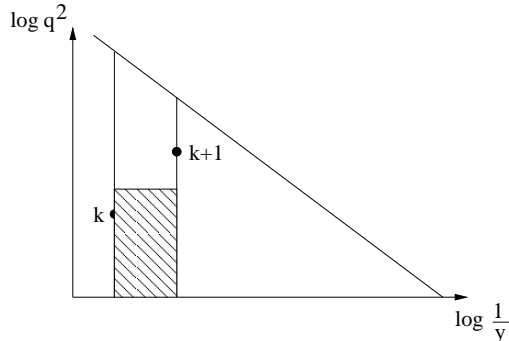


Figure 3: The shaded region is the region left over where there is a net contribution from the virtual form factors. It is bounded from above by  $Q_k$ . The real emissions are represented by fat dots.

positive in  $S_{ne}(k)$ , we get a complete cancelation in the region of overlap. It is then easy to see from Fig. 2 that the region which is left is the one shown in Fig. 3, and that the net exponent is negative.

Now, remember that in the BFKL evolution, the virtual corrections are contained in the “non-Sudakov” (or “non-eikonal”) factor  $\Delta_{ne}^{BFKL}(k)$  defined by

$$\Delta_{ne}^{(BFKL)}(k) = \exp \left( -\bar{\alpha}_s \int_{y_{k+1}}^{y_k} \frac{dy}{y} \int_{q_0^2}^{Q_k^2} \frac{dq^2}{q^2} \right), \quad (2.6)$$

and we see that this corresponds to the shaded area in Fig. 3. Thus we find

$$S_{ne}^2(k) \cdot S_{eik}^2(k) = \Delta_{ne}^{BFKL}(k). \quad (2.7)$$

Consider now a complete set of emissions in the initial chain as shown in Fig. 4. In the figure the gluons are obviously enumerated according to their energy. The explanation of the phase space in figure is the following. The  $Q_i$  are determined by the relation  $Q_i = -\sum_k^i q_k$ . For example, since  $Q_0 = 0$ , we have  $Q_1 = q_1$  (in the following all the momenta denote the norm of the transverse components). Since  $q_2 \gg q_1$  we have  $Q_2 \simeq q_2$ , where the small recoil is neglected in the figure. Then the subsequent real gluons have small momenta so that  $Q_{k+1} \approx Q_k$  up to gluon 6 which has large momentum, and therefore  $Q_6 \simeq q_6$  and so on. In the end we get an integral over the total shaded region in Fig. 4, and again this is exactly the same that we would have in BFKL.

Of course in CCFM the total phase space is determined by  $\bar{\xi}$  so in Fig. 4 we have assumed the constraint  $\xi < \bar{\xi}$  not to cut the shaded regions. Hence, a difference between the CCFM and BFKL ladder appears towards the end of the chain. This difference however is not enhanced by  $\ln(1/x)$ , and hence it is subleading from the viewpoint of the BFKL resummation. Moreover, the CCFM real-gluon emissions are ordered according to their angle, and not to the energy. However, in the ensuing gluon distribution (2.2) there is a sum over all the possible angular orderings for a given energy ordering. Therefore the phase space for real emissions is also the same, up to the subleading difference mentioned above.

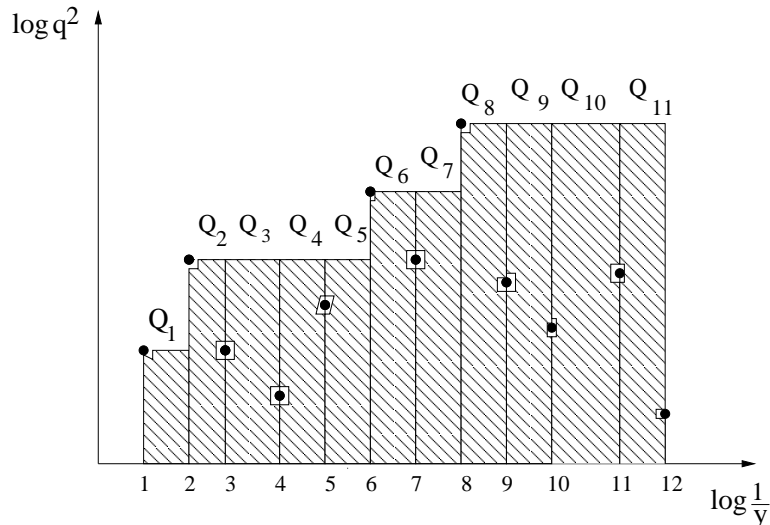


Figure 4: A complete set of emissions in the CCFM phase space. Real emissions are represented by fat dots. The shaded regions are the regions over which we have contributions from the virtual form factors. We have here ignored the constraint from the maximal angle.

In general, however, the energy weighting of the real and virtual emissions is different for the BFKL and CCFM evolutions. For the latter, this is encoded in the splitting functions in Eqs. (2.2) and (2.3)–(2.4), which show that the (real and virtual) gluon emissions are distributed logarithmically in  $y$  — the rapidity of the  $s$ -channel gluons. The BFKL evolution, on the other hand, retains those diagrams which resum all orders in  $\alpha_s \ln(1/x)$ : these are gluon ladders in which the  $t$ -channel gluons are strongly ordered in longitudinal momentum ( $x = x_n \ll x_{n-1} \ll \dots \ll x_1 \ll x_0$ ) and distributed with the logarithmic weight  $dx_i/x_i$ . Clearly, strong ordering in the  $t$ -channel implies a similar ordering in the  $s$ -channel — from  $x_i \ll x_{i-1}$ , it follows that  $y_i \simeq x_{i-1} \ll y_{i-1} \simeq x_{i-2}$  —, so that the positions (in energy) of the  $t$ -channel propagators uniquely determine the positions of the real gluons. This is true in the strict high energy limit, where  $s \rightarrow \infty$  at fixed  $Q^2$ , and  $\bar{\alpha}_s$  is very small. Beyond this, however, it is important that the CCFM configurations are generated according to the rule of quantum coherence, and hence they represent realistic final states (at least, up to further emissions from the real CCFM gluon, as explained at the end of Sect. 2.1). Thus, although the two types of evolution provide identical results for the (inclusive) gluon distribution in the formal high-energy limit the CCFM evolution is more appropriate for describing actual final states (see the discussion at the end of section 2.3). Moreover, this *formal* high-energy limit becomes meaningless in the presence of saturation, as we shall later explain, and when this limit is properly taken (see in Sect. 4), differences are expected to appear already in inclusive quantities, so like the gluon distribution.

### 2.3. The structure of the angular ordered cascade

Returning to Eq. (2.2), this can be further simplified to obtain a more familiar expression for the gluon distribution. To that aim, we shall divide the initial state radiation into

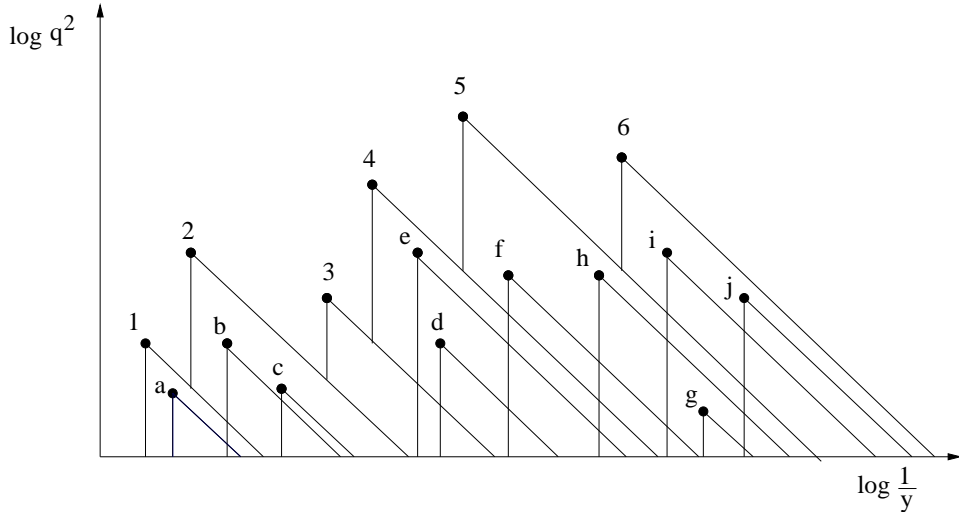


Figure 5: Dividing the CCFM radiation into two subsets: hard emissions (enumerated emissions) and soft emissions (indexed by small letters) as explained in the text. All real emissions are represented by fat dots.

two classes, “soft” and “hard” (or “fast”) gluons [4]. This is done as follows. Consider the set of initial gluons shown in Fig. 5. The “hard” subset of gluons are those which are not in angle followed by a gluon with more energy, *i.e.* with higher  $y$ . All other gluons are defined as being “soft” gluons. In Fig. 5, the gluons marked by 1, 2, 3, 4, 5 and 6 are hard gluons, since as compared to them, there are no other gluons with larger angle and higher energy. (Recall that a larger angle would mean a gluon above the respective diagonal line, while a higher energy means a gluon to the left of the vertical line through the gluon.) The gluons marked by  $a, b, c, d, e, f, g, h, i$  and  $j$  are soft gluons. For example,  $a$  is in angle followed by 1 and 1 has larger energy than  $a$  since it is located to the left of it. Gluon  $d$  is followed by  $e$  which has larger energy, which itself is followed by 4 in angle which has also larger energy than  $e$ . The hard gluons are thus ordered *both* in angle and in energy.

The soft gluons can furthermore be divided into clusters. Define the cluster  $C_k$  as consisting of those soft gluons which have their angle between  $\xi_{k-1}$  and  $\xi_k$ , and which have energies less than  $y_k$ . Thus in Fig. 5,  $a$  belongs to cluster  $C_1$  since  $0 < \xi_a < \xi_1$  ( $\xi_0 \equiv 0$ ) and  $y_a < y_1$ ,  $b$  and  $c$  belong to  $C_2$  since  $\xi_1 < \xi_{b,c} < \xi_2$  and so on. In this example there are no gluons in  $C_3$ . The phase spaces for the clusters  $C_i$  are shown in Fig. 6. We now see that the “soft” gluons which belong to the cluster  $C_k$  are indeed soft in the sense of having lower energies than the “hard” gluon  $k$  which defines the cluster.

The advantage of this separation is that it allows us to rewrite the distribution (2.2) in a simpler way. To that aim, notice that the soft gluons in  $C_k$  have all transverse momenta smaller than  $q_k$ . This is obvious from the figures and more formally follows from the fact

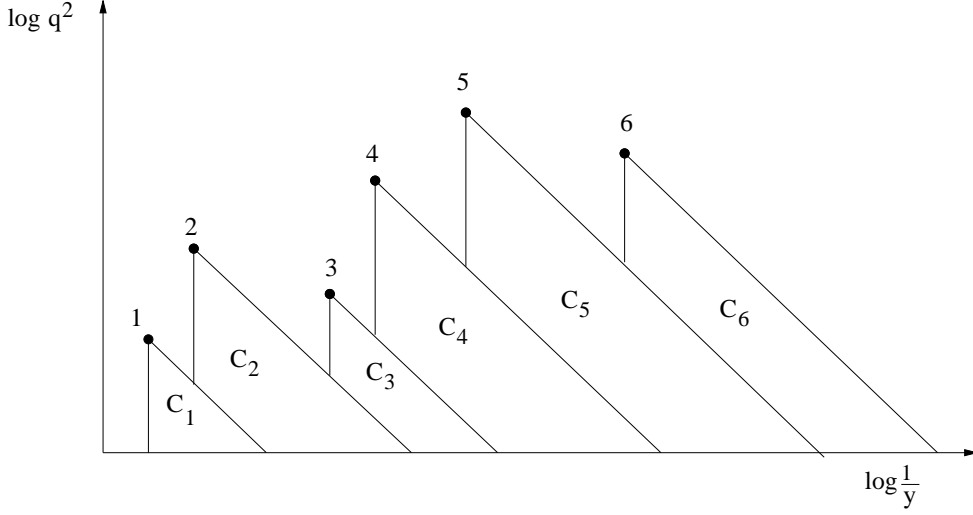


Figure 6: The representation of the hard emissions, enumerated fat dots, together with the clusters  $C_i$ . For each hard emission  $i$ , the cluster  $C_i$  contains all the soft emissions associated with that hard emission.

that<sup>3</sup>  $\xi_{s,k} < \xi_k$  and  $y_{s,k} < y_k$  implies  $q_{s,k}^2 < (y_{s,k}^2/y_k^2)q_k^2 < q_k^2$ . Then one can write

$$S_{ne}^2 = \prod_{k \in \mathcal{A}} S_{ne}^2(k) \approx \prod_{k \in \mathcal{H}} S_{ne}^2(k) \quad (2.8)$$

where  $\mathcal{A}$  denotes the set of all emissions while  $\mathcal{H}$  denotes the subset of hard emissions, and the phase-space for a hard gluon in  $\mathcal{H}$  is the whole respective cluster  $C_k$ , as shown in Fig. 6. The gluon distribution (2.2) can then be written as

$$\begin{aligned} \mathcal{A}(x, \bar{\xi}) &= \sum_{n=1}^{\infty} \int \prod_{k=1}^n \left( \bar{\alpha}_s \frac{dy_k}{y_k} \frac{d\xi_k}{\xi_k} S_{ne}^2(y_{k+1}, y_k, Q_k) \theta(\xi_{k+1} - \xi_k) \theta(y_k - y_{k+1}) \right) \frac{1}{x_n} \delta(x - x_n) \\ &\times S_{eik}^2(y_1, \bar{\xi}) \prod_{k=1}^{n+1} \left( \sum_{m=0}^{\infty} \bar{\alpha}_s^m \int_{C_k} \prod_{i=1}^m \frac{dy_i}{y_i} \frac{d\xi_i}{\xi_i} \theta(\xi_{i+1} - \xi_i) \right). \end{aligned} \quad (2.9)$$

where  $\xi_{n+1} \equiv \bar{\xi}$ , and we now index the gluons by using the angular ordering. The meaning of this equation is simple: it says that we can construct each chain by adding an arbitrary number of soft gluons between each pair of hard emissions. We can now further simplify this expression, by using cancelations between real and virtual contributions to the emission of the soft gluons.

To that purpose, we refer to Fig. 7 where we have identified the hard and soft emissions from Fig. 5, and the numerated emissions are the hard ones. For these we also indicate the angles. The soft gluons are marked by small letters. We now define the new “non–

<sup>3</sup>We denote by  $\xi_{s,k}$  and  $y_{s,k}$  the angle and energy fraction for a soft gluon belonging to cluster  $C_k$ .

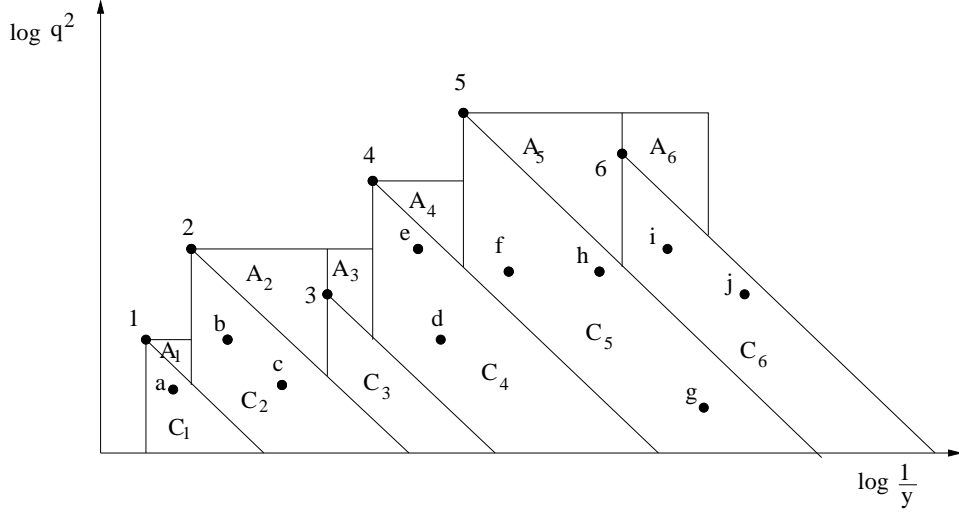


Figure 7: The hard and soft emissions, represented by fat dots, in CCFM together with the phase space regions for the “non-Sudakov” (regions  $A_i$ ) and the “Sudakov” (regions  $C_i$ ) form factor. The Sudakov cancels the real soft emissions.

Sudakov” form factor  $\Delta_{ns}$  by

$$\Delta_{ns} = \prod_k \Delta_{ns}(k) = \prod_k \exp(-\bar{\alpha}_s A_k). \quad (2.10)$$

Similarly we define the “Sudakov” factors  $\Delta_s(k)$  by

$$\Delta_s = \prod_k \Delta_s(k) = \prod_k \exp(-\bar{\alpha}_s C_k). \quad (2.11)$$

Thus we have

$$S_{eik}^2(y_1, \bar{\xi}) \cdot \prod_k S_{ne}^2(k) = \prod_k \Delta_{ns}(k) \cdot \Delta_s(k). \quad (2.12)$$

Now, the summation over the real soft emissions in each cluster  $C_k$  in (2.9) exponentiates,

$$\sum_{m=0}^{\infty} \bar{\alpha}_s^m \int_{C_k} \prod_{i=1}^m \frac{dy_i}{y_i} \frac{d\xi_i}{\xi_i} \theta(\xi_{i+1} - \xi_i) = \exp(\bar{\alpha}_s C_k) \equiv \Delta_R^{soft}(k). \quad (2.13)$$

By the definition of the Sudakov in (2.11) we thus have

$$\Delta_s(k) \cdot \Delta_R^{soft}(k) = 1, \quad (2.14)$$

*i.e.* the real soft emissions are exactly compensated by the Sudakov form factors. After thus inclusively summing over all soft emissions, the structure function can be finally

written as

$$\mathcal{A}(x, \bar{\xi}) = \sum_{n=1}^{\infty} \int \prod_{k=1}^n \left( \frac{dy_k}{y_k} \frac{d\xi_k}{\xi_k} \Delta_{ns}(y_{k+1}, y_k, Q_k) \theta(\xi_{k+1} - \xi_k) \theta(y_k - y_{k+1}) \right) \frac{1}{x_n} \delta(x - x_n). \quad (2.15)$$

This expression involves the *hard* gluons alone.

Before leaving this section, two comments are in order:

(i) In Fig. 7 the horizontal lines between the real emissions represent the momenta of the  $t$ -channel gluons. As obvious from the figure, these momenta are determined solely by the hard subset of emissions (*c.f.* Eq. (2.8)) which are ordered *in both* energy and angle. This *a posteriori* explains why the condition  $Q_i = -\sum_k^i q_k$  is approximately true irrespective whether the labels  $i, k$  refer to energy ordering, or to the angular ordering (which is the actual order of the gluon emissions). This argument shows that there is an implicit approximation in the CCFM formalism — the fact that soft gluon emissions are assumed not to change the virtual transverse momenta. Hence, without further loss of accuracy, we will later use similar approximations to simplify the expression of the gluon distribution even further (see Sect. 3).

The second important point is the relation to BFKL mentioned earlier and which deserves some clarifications. To compare to BFKL, it is convenient to define  $z_k$  by  $x_k \equiv z_k x_{k-1}$ . This implies  $y_k = x_{k-1}(1 - z_k)$ , and therefore

$$\frac{1}{x_n} \prod_k \frac{dy_k}{y_k} = \prod_k \frac{dz_k}{z_k(1 - z_k)} = \prod_k dz_k \left( \frac{1}{z_k} + \frac{1}{1 - z_k} \right). \quad (2.16)$$

Thus in the CCFM ladder one can distinguish two vertices contributing to the splitting  $Q_{k-1} \rightarrow q_k + Q_k$ . The one corresponding to the small- $z_k$  pole  $1/z_k$  is dubbed the “non-eikonal” vertex as it comes from the piece of the three gluon vertex in which the polarization of the parent gluon is inherited by the real gluon  $q_k$ . The opposite  $1/(1 - z_k)$  pole is dubbed the “eikonal” vertex, and in this case the polarization, together with most of the energy, is inherited by the  $t$ -channel propagator  $Q_k$ . The hard emissions previously identified are associated with the  $1/z_k$  pole in Eq. (2.16), while the soft emissions with the  $1/(1 - z_k)$  pole [4]. In contrast, in a BFKL ladder, only the  $1/z_k$  pole would be present, and the energy ordering coincides with the actual sequence of emissions along the cascade. In that case the typical gluons are such that  $z_k \ll 1$  and hence  $y_k \simeq x_{k-1}$ , as anticipated at the end of Sect. 2.2. Thus in the corresponding phase-space integrals, like Eq. (2.6), one can replace the measure  $dy_k/y_k$  by  $dz_k/z_k$ . We are now prepared for our second comment:

(ii) Despite the formal equivalence between the CCFM and BFKL evolutions (in the high energy limit), the latter cannot be used to generate the final state, not only because it does not obey the condition of angular ordering (as required by quantum coherence), but also because the Regge kinematics  $z_k \ll 1$  cannot be ensured in practice when trying to generate a BFKL ladder. The reason is as follows: the BFKL emission probabilities for real and, respectively, virtual gluons are separately infrared divergent (see e.g. Eq. (2.6)) and thus require an infrared regulator  $q_0$ . Although the dependence upon  $q_0$  formally cancels in the complete result, the introduction of this soft momentum cutoff will falsify

the condition that  $z_k \ll 1$  in the intermediate steps. Indeed, when a new value for  $z_k$  is randomly generated with probability law  $\Delta_{ne}^{(BFKL)}(k)$ , the typical value value is such that

$$\ln \frac{1}{z_k} \sim \frac{1}{\bar{\alpha}_s} \frac{1}{\ln(Q_k^2/q_0^2)}, \quad (2.17)$$

which in principle should be of  $\mathcal{O}(1/\bar{\alpha}_s)$  for the Regge kinematics to apply, but in reality becomes of  $\mathcal{O}(1)$  (meaning  $z_k \sim \mathcal{O}(1)$  as well) whenever  $q_0$  is taken to be small enough.

Within the CCFM evolution, this problem is avoided due to the presence of both types of poles,  $1/z_k$  and  $1/(1-z_k)$ , and to the angular ordering. In that context, the dependence on  $q_0$  is present in the Sudakov form factor, as the areas  $C_k$  in Fig. 7 are cut from below by  $q_0$ . In the  $q_0 \rightarrow 0$  limit, successive emissions will become very close to each other in angle. Indeed, an emission typically occurs when the corresponding region  $C_k$  (that we now define separately for *each* emission, either hard, or soft; see Fig. 8) has an area of  $\mathcal{O}(1)$ ,

$$\bar{\alpha}_s \ln \left( \frac{q_k^2}{q_0^2} \sqrt{\frac{\xi_{k-1}}{\xi_k}} \right) \ln \sqrt{\frac{\xi_k}{\xi_{k-1}}} \sim 1, \quad (2.18)$$

which implies  $\xi_k \rightarrow \xi_{k-1}$  when  $q_0 \rightarrow 0$ . In that case one can identify two limiting cases: (i)  $z \ll 1$  and  $q$  more or less similar to the momentum of the previous emission, or (ii)  $z \approx 1$  and  $q$  either of the order of, or much smaller than, the  $q$  of the previous emission. These two possibilities are precisely the type of emissions already present in CCFM and therefore the structure of the cascade is not altered by  $q_0$ , unlike what happens in BFKL.

Of course, in the presence of saturation the dependence on any soft momentum disappears naturally, as the dynamically generated saturation momentum, which grows rapidly in the course of the evolution, provides a natural cutoff (see the discussion in Sect. 4.1).

#### 2.4. The virtual form factors

In this subsection we shall display some more explicit formulæ for the non-Sudakov and Sudakov form factors  $\Delta_{ns}$  and  $\Delta_s$ , whose detailed derivation is presented in appendix A. Although such formulæ were already presented in the original work [4], it turns out that they are often written in a wrong way in the literature (see the discussion in appendix A). To avoid such errors, and also in order to be able to generalize these form factors by including non-leading effects — a task that we address in appendix B —, it is essential to have a proper understanding of the derivation of the corresponding formulæ. This is briefly discussed here and then in more detail in appendix A.

Let us first recall that for the hard emissions,  $y_k = (1-z_k)x_{k-1} \approx x_{k-1}$ , while for the soft emissions  $x_k = z_k x_{k-1} \approx x_{k-1}$ . Then one can as a first approximation set  $z_k = 0$  for the hard emissions (except in the  $1/z_k$  pole), and  $z_k = 1$  for the soft emissions (except in the  $1/(1-z_k)$  pole). Therefore the region  $A_k$  has the transverse momentum bounded from below by  $\xi_k$ , and from above by  $Q_k$ , while the respective  $y$  integral is bounded between  $y_k$  and  $y_{k+1}$ . Thus we approximately have

$$\Delta_{ns}(k) = \exp \left( -\bar{\alpha}_s \int_{x_k}^{x_{k-1}} \frac{dy}{y} \int_{\xi_k}^{Q_k^2/(y^2 E^2)} \frac{d\xi}{\xi} \right). \quad (2.19)$$

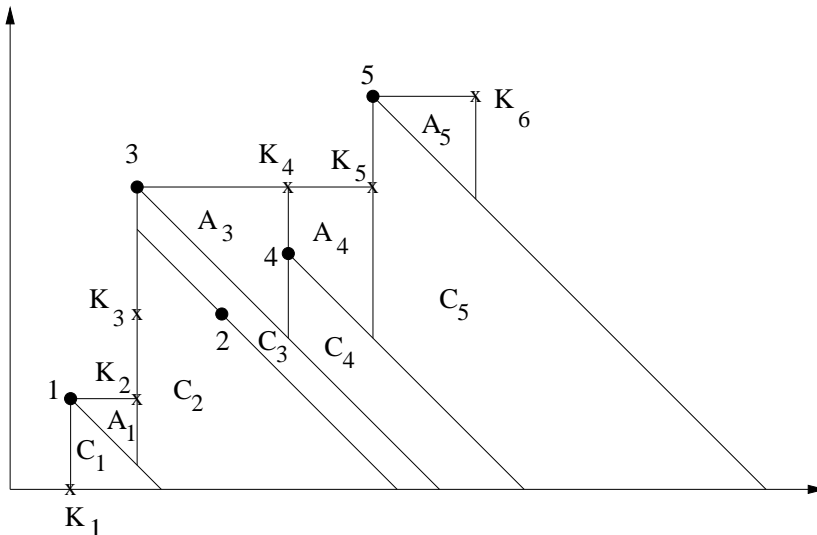


Figure 8: *Hard and soft emissions, with the Sudakov (regions  $C_i$ ) defined for each individual emission. To leading order there is no non-Sudakov (regions  $A_i$ ) associated with the soft emissions. Real emissions are again represented by fat dots, while the  $k_\perp$  and energy fraction of the virtual propagators are denoted by crosses. In this example, emission number 2 is a soft emission.*

Defining  $y \equiv z x_{k-1}$ , and switching from  $\xi$  to  $q$  by using  $\xi = q^2/(y^2 E^2)$  one gets

$$\Delta_{ns}(k) = \exp \left( -\bar{\alpha}_s \int_{z_k}^1 \frac{dz}{z} \int_{z^2 q_k^2 / (1-z_k)^2}^{Q_k^2} \frac{dq^2}{q^2} \right). \quad (2.20)$$

The reason we did not set  $1 - z_k = 1$  in the lower limit of the  $q$  integral is because the CCFM equation is usually written in terms of the so-called rescaled momenta defined by  $p_k \equiv q_k/(1 - z_k)$  so that the factor  $(1 - z_k)$  is absorbed into the definition of  $p_k$ . Then

$$\Delta_{ns}(k) = \exp \left( -\bar{\alpha}_s \int_{z_k}^1 \frac{dz}{z} \int_{z^2 p_k^2}^{Q_k^2} \frac{dq^2}{q^2} \right) \quad (2.21)$$

which is the form used in [4]. Equation 2.21 for  $\Delta_{ns}$  is, however, usually written in a different way in the literature (see Eq. (A.1) in the appendix). In appendix A, we give a more careful derivation of the non-Sudakov form factor, and we demonstrate that the correct form is indeed given by 2.21.

To write down the Sudakov one first needs to define it for each, hard and soft, individual emission. In Fig. 8 we show an explicit chain of hard and soft emissions, where the real emissions are indexed according to their angular ordering, and where we also explicitly show the virtual t-channel propagators by crosses. The individual Sudakov form factors are then defined as the integrals over the regions  $C_k$  in the figure (note that these are not the same regions  $C_k$  as before, now we define such a region for each emission, not just for the hard ones).



We see that the region  $C_k$  is to the left bounded by the energy of  $Q_{k-1}$ , while there is no lower limit for the energy<sup>4</sup>. In momenta it is bounded between the angles of the real gluons  $q_{k-1}$  and  $q_k$ . Therefore we may write the Sudakov as

$$\Delta_s(k) = \exp \left( -\bar{\alpha}_s \int_{\xi_{k-1}}^{\xi_k} \frac{d\xi}{\xi} \int_{\epsilon}^{x_{k-1}} \frac{dy}{y} \right) \quad (2.22)$$

where  $\epsilon$  represents the soft cutoff. Since we must have  $q > q_0$  we get  $\xi = q^2/(y^2 E^2) > q_0^2/(y^2 E^2)$  and  $y > q_0/(\sqrt{\xi} E) = \epsilon$ . Defining  $p = \sqrt{\xi} x_{k-1} E$ , we have  $\epsilon = x_{k-1} q_0/p$  and

$$\Delta_s(k) = \exp \left( -\bar{\alpha}_s \int_{z_{k-1}^2 p_{k-1}^2}^{p_k^2} \frac{dp^2}{p^2} \int_{\epsilon'}^1 \frac{dy}{y} \right). \quad (2.23)$$

where  $\epsilon' = \epsilon/x_{k-1} = q_0/p$ . Now if one wishes one can let  $y = 1 - z$  and then the usual form for the Sudakov form factor is obtained.

### 3. More inclusive versions of CCFM

In section 2.3 we have shown that one can use the Sudakov form factors to cancel the real soft emissions, and this resulted in a simplified expression for the gluon distribution, Eq. (2.15). This distribution is more “inclusive” than the original one, Eq. (2.2), which explicitly includes all soft emissions, yet it is equivalent to it for the calculation of the gluon distribution. In this section, we shall construct other, even more inclusive, versions of the CCFM evolution, which are better adapted for numerical calculations. In these constructions, we shall exploit the flexibility which exists in defining the CCFM evolution, as associated with the various approximations involved in its derivation. Note that “getting more inclusive” is not the only possibility for deriving different versions of CCFM. In appendix B we shall derive yet another version by including non-leading effects related to recoils. That version could be implemented in a Monte Carlo simulation, so like CASCADE.

#### 3.1. Integral equations

From now on we shall work with the ‘unintegrated’ gluon distribution, i.e., the number of gluons with a given longitudinal momentum fraction  $x$  and a given transverse momentum  $k$ , which is obtained by undoing the integral over the last angular variable  $\xi_n$  in Eq. (2.2) (or (2.9)) and replacing  $\xi_n \rightarrow k^2/x^2 E^2$ . It will be also convenient to replace the maximal angle  $\bar{\xi}$  by a corresponding momentum variable  $\bar{q}$ , via the substitution  $\bar{\xi} = \bar{q}^2/(x^2 E^2)$ ; as explained after Eq. (2.2), one has roughly  $\bar{q}^2 \simeq Q^2$  (the virtuality of the space-like photon exchanged in DIS). The integral equation satisfied by  $\mathcal{A}(x, k, \bar{q})$  is

---

<sup>4</sup>Eventually there will be a limit coming from the soft momentum cut, so that the region does not extend to infinite size

easy to derive from Eq. (2.9), and reads

$$\mathcal{A}(x, k, \bar{p}) = \bar{\alpha}_s \int_x^1 dz \int \frac{d^2 p}{\pi p^2} \theta(\bar{p} - zp) \Delta_s(\bar{p}, zp) \left( \frac{\Delta_{ns}(k, z, p)}{z} + \frac{1}{1-z} \right) \times \mathcal{A} \left( \frac{x}{z}, |k + (1-z)p|, p \right), \quad (3.1)$$

where we are using rescaled momenta within the integrand:  $\bar{p} = \bar{q}/(1-x)$  and  $p = q/(1-z)$ . The third argument of the gluon distribution inside the integrand, *i.e.*  $p$ , truly means that the maximal angle corresponding to this distribution is the angle  $\xi$  of the emitted real gluon, that is,  $\xi = q^2/(y^2 E^2) = z^2 p^2/x^2 E^2$ , with  $y = (1-z)(x/z)$ . Hence, this equation can be read as follows: the final  $t$ -channel gluon with energy fraction  $x$  and transverse momentum  $k$  (and for a maximum emission angle measured by  $\bar{q}$ ) is generated via the splitting  $k' \rightarrow k + q$  of a previous  $t$ -channel gluon with energy fraction  $x/z > x$  and transverse momentum  $|k'| = |k + q|$  (and for a maximum emission angle measured by  $p$  and  $z$ ). This is the most exclusive version of the integral equation and includes all the hard and soft emissions. This equation is implemented in the CASCADE event generator [13].

In the more inclusive version we can sum over all soft emissions (in the regions  $C_i$  in Fig. 6) so that the Sudakov factors disappear and we are left with the gluon distribution in Eq. (2.15). This version gives rise to the following integral equation

$$\mathcal{A}(x, k, \bar{p}) = \bar{\alpha}_s \int_x^1 \frac{dz}{z} \int \frac{d^2 p}{\pi p^2} \theta(\bar{p} - zp) \Delta_{ns}(k, z, p) \mathcal{A} \left( \frac{x}{z}, |k + (1-z)p|, p \right). \quad (3.2)$$

This equation is simpler to solve than (3.1) but is still not very easy to deal with, not even numerically. Notice that one might as well use Eq. (3.2) as the basis for an event generator, but then all soft emissions must later be included as final state radiation. In what follows, however, we shall be concentrating on the small- $x$  part of the gluon distribution, where the small- $z$  values ( $z \ll 1$ ) are dominating. In that case one can replace all rescaled momenta with regular momenta, and rewrite  $|k + (1-z)p| \rightarrow |k + q|$  in the argument of  $\mathcal{A}$  within the integrand; also the energy ordering becomes automatic. Hence the equation becomes

$$\mathcal{A}(x, k, \bar{q}) = \bar{\alpha}_s \int_x^1 \frac{dz}{z} \int \frac{d^2 q}{\pi q^2} \theta(\bar{q} - zq) \Delta_{ns}(k, z, q) \mathcal{A} \left( \frac{x}{z}, |k + q|, p \right), \quad (3.3)$$

### 3.2. Geometrical representation of the real vs. virtual cancelations

Starting with Eq. (3.3), we shall later derive the most inclusive, and also the simplest, version of the CCFM equation. To that aim it is important to understand in depth the structure of the virtual corrections encoded in the ‘non-Sudakov’ form factor  $\Delta_{ns}$ , Eq. (2.10). Note first that, despite its name, this form factor is essentially not different from a genuine Sudakov one, since it also represents the negative exponent of an area in the phase space, namely the areas  $A_i$  in figures 7 and 8. It can therefore be used to cancel the real emissions confined to this phase space, as was first noted in [30]. As we review in appendix A however, this is strictly true only if the additional kinematical constraint

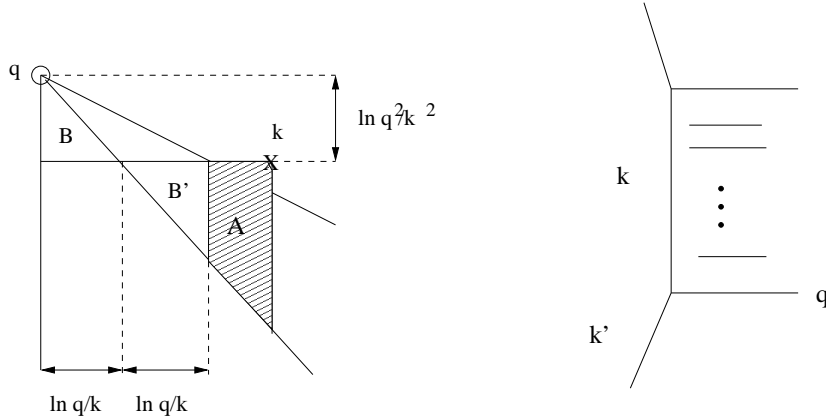


Figure 9: The phase space for  $\Delta_{ns}$ . The region  $B$  contributes with negative weight, and it is seen that  $B = B'$ . The shaded region  $A$  is thus the region left over, which is also the region to which the (real)  $k_{\perp}$ -conserving emissions are confined. To the right we show symbolically the insertion of  $k_{\perp}$ -conserving emissions between a pair of non- $k_{\perp}$ -conserving emissions. The propagator  $k$  is unchanged by this insertion.

$k^2 > zq^2$ , which ensures that the squared 4-momenta of the  $t$ -channel propagators are dominated by their transverse part [4, 40], is enforced within (3.3).

Assuming  $k^2 > zq^2$  from now on, we can distinguish between two cases:  $k \geq q$  and  $k < q$ . When  $k \geq q$ , the regions  $A_i$  in figures 7 and 8 correspond to real emissions with  $q \ll k \approx k'$  and  $\Delta_{ns}$  is guaranteed to be smaller than 1. Consider now the situation in Fig. 9 where  $k < q$ . As we show in appendix A, we have

$$\Delta_{ns} = \exp(-\bar{\alpha}_s(A + B' - B)) \quad (3.4)$$

where the regions  $A$  (shaded region),  $B$  and  $B'$  are shown in Fig. 9. The first observation is that the triangular regions  $B$  and  $B'$  have the same area, and hence they cancel in the exponent of Eq. (3.4). The upper diagonal line in Fig. 9 indicates the line through which the kinematical constraint limit  $k^2 = zq^2$  holds, while the lower diagonal line indicates the angle of  $q$ . Now, the emissions lying below  $k$  are, in the spirit of the approximations made in section 2.3,  $k_{\perp}$ -conserving. When the kinematical constraint is included, these emissions are confined to the shaded region (region  $A$ ) in figure 9. This can be understood as follows: due to angular ordering and the fact that we are looking at  $k_{\perp}$ -conserving emissions, all subsequent radiation must lie in the region  $B'$  or in  $A$ . However, if we had a real emission in region  $B'$ , then because that emission is  $k_{\perp}$ -conserving, the  $t$ -channel propagator emitting this gluon would have transverse momentum approximately equal to  $k$  and it would necessarily have bigger energy than the real gluon. Therefore we see that it must be located under the upper diagonal line in Fig. 9. This, however, would violate the kinematical constraint and such an emission is therefore not possible. Thus we are left with the fact that all real  $k_{\perp}$ -conserving emissions are confined to region  $A$ . Therefore the inclusive summation over all the real emissions, which are inserted in between two non- $k_{\perp}$ -conserving emissions, leads to a factor

$$\Delta_R = \exp(\bar{\alpha}_s A). \quad (3.5)$$

To conclude (recall that  $B' = B$ )

$$\Delta_R \cdot \Delta_{ns} = \exp(\bar{\alpha}_s(A - A + B - B)) = 1 \quad (3.6)$$

which shows that the ‘‘non-Sudakov’’ factor cancels the  $k_\perp$ -conserving emissions. This was first noticed in [30], and it was later used in [38] as well<sup>5</sup>. One is then left with a much simpler formula for  $\mathcal{A}$  which can be derived from Eq. (3.2) after including the constraint  $k^2 > zq^2$ , and the fact that we are left only with the non- $k_\perp$ -conserving emissions. This last constraint, however, can be enforced in various ways, which are all consistent with each other within the present approximations. Therefore there is no unique equation that one can derive. In what follows we shall consider two different possibilities and then study the ensuing equations.

### 3.3. Deriving the differential equations

In Ref. [1] we have the restriction to non- $k_\perp$ -conserving emissions by introducing the theta function  $\theta(q^2 - \min(k^2, k'^2))$  into the r.h.s. of the integral Eq. (3.3). This was also the prescription originally used in Ref. [30], and the equations derived in [1] and [30] are indeed equivalent. After inserting this constraint together with the ‘kinematical’ one  $k^2 > zq^2$  and removing  $\Delta_{ns}$ , Eq. (3.3) becomes

$$\mathcal{A}(x, k, \bar{q}) = \bar{\alpha}_s \int_x^1 \frac{dz}{z} \int \frac{d^2q}{\pi q^2} \theta(\bar{q} - zq) \theta(k^2 - zq^2) \theta(q^2 - \min(k^2, k'^2)) \mathcal{A}\left(\frac{x}{z}, k', q\right). \quad (3.7)$$

Since  $\bar{q} \geq k$  for all cases of physical interest (recall that  $\bar{q}^2 \simeq Q^2$  in DIS), we further have  $\bar{q}^2 \geq k^2 \geq zq^2 \geq z^2q^2$ . Therefore the angular ordering is automatic and  $\theta(\bar{q} - zq)$  can be neglected. This means that the dependence on the third variable  $\bar{q}$  drops out, at least in the l.h.s. But a similar argument holds also for the function for  $\mathcal{A}(x/z, k', q)$  under the integral, because we have  $q \geq k'$  (indeed, we are left only with emissions satisfying  $k' \approx q \gg k$  or  $k \approx q \gg k'$ ). Dropping then the dependence of  $\mathcal{A}$  upon its third variable, we obtain

$$\mathcal{A}(x, k) = \bar{\alpha}_s \int_x^1 \frac{dz}{z} \int \frac{d^2q}{\pi q^2} \theta(k^2 - zq^2) \theta(q^2 - \min(k^2, k'^2)) \mathcal{A}\left(\frac{x}{z}, k'\right). \quad (3.8)$$

The next step is to perform the integration over the azimuthal angle  $\phi$ . To that aim, it is convenient to replace  $\theta(k^2 - zq^2)$  by  $\theta(k^2 - zk'^2)$ , which is allowed within the current approximations<sup>6</sup>, and then switch the integration variables from  $q$  to  $k'$  and, respectively, from  $z$  to  $x/z$  (which we rename as  $z$ ). Making this replacement and doing the  $\phi$  integral one then gets

$$\mathcal{A}(x, k) = \bar{\alpha}_s \int_x^1 \frac{dz}{z} \int \frac{dk'^2}{|k'^2 - k^2|} \theta(z - xk'^2/k^2) h(\kappa) \mathcal{A}(z, k'), \quad (3.9)$$

<sup>5</sup> In [38], however, only the possibilities  $k' \approx k \gg q$  and  $k \approx q \gg k'$  were considered. In that case there is obviously no need for the kinematical constraint.

<sup>6</sup> Indeed, we have either  $k' \approx q \gg k$ , in which case the replacement is obviously correct, or  $k \approx q \gg k'$ , in which case both the first and the second theta function can be replaced by 1.

where

$$h(\kappa) = 1 - \frac{2}{\pi} \arctan \left( \frac{1 + \sqrt{\kappa}}{1 - \sqrt{\kappa}} \sqrt{\frac{2\sqrt{\kappa} - 1}{2\sqrt{\kappa} + 1}} \right) \theta(\kappa - 1/4). \quad (3.10)$$

and  $\kappa \equiv \min(k^2, k'^2)/\max(k^2, k'^2)$ . Differentiating w.r.t to  $Y$  we finally deduce the following differential equation for the unintegrated gluon distribution in the CCFM formalism

$$\begin{aligned} \partial_Y \mathcal{A}(Y, k) = \bar{\alpha}_s \int \frac{dk'^2}{|k^2 - k'^2|} h(\kappa) & \left( \theta(k^2 - k'^2) \mathcal{A}(Y, k') \right. \\ & \left. + \theta(k'^2 - k^2) \theta(Y - \ln(k'^2/k^2)) \mathcal{A}(Y - \ln(k'^2/k^2), k') \right). \end{aligned} \quad (3.11)$$

As mentioned above, (3.11) is equivalent to the master equation in the LDC formalism [30] (up to some trivial redefinitions: the distribution in [30] corresponds to our  $k^2 \mathcal{A}(Y, k)$  times the proton radius and some constants).

Yet another way to implement the restriction to non- $k_\perp$ -conserving emissions is to switch the integration variable in Eq. (3.3) from  $q$  to  $k' = |q + k|$  and then replace  $q^2$  with  $\max(k^2, k'^2)$ . Note that this constraint is more restrictive than the theta function in Eq. (3.7). In this case the angular integration in (3.7) becomes trivial. Also the replacement  $\theta(k^2 - zq^2) \rightarrow \theta(k^2 - zk'^2)$  is now exact, and so is also the requirement  $q \geq k'$  (which, we recall, allows one to ignore the dependence of  $\mathcal{A}(x, k, \bar{q})$  upon its third, ‘maximal angle’, variable). We thus deduce

$$\begin{aligned} \partial_Y \mathcal{A}(Y, k) = \bar{\alpha}_s \int \frac{dk'^2}{\max(k^2, k'^2)} & \left( \theta(k^2 - k'^2) \mathcal{A}(Y, k') \right. \\ & \left. + \theta(k'^2 - k^2) \theta(Y - \ln(k'^2/k^2)) \mathcal{A}(Y - \ln(k'^2/k^2), k') \right). \end{aligned} \quad (3.12)$$

### 3.4. More on the relation to BFKL

Before moving on to discuss the issues of unitarity and saturation, we would like to discuss the effects of the kinematic constraint on the BFKL equation, and we would like to show that the same approximations used above in deriving the more inclusive equations (3.11) and (3.12) applied on BFKL, with the kinematical constraint, leads exactly to the same equations. In section 5 we will present numerical results of the BFKL equation with the kinematic constraint included, with and without the saturation boundary to be described in the next section.

The BFKL equation can be written

$$\mathcal{A}(Y, k) = \bar{\alpha}_s \int_0^Y dy \int \frac{d^2q}{\pi q^2} \theta(Y - y + \ln(k^2/k'^2)) \Delta'(Y - y, k) \mathcal{A}(y, k') \quad (3.13)$$

where we have included the kinematical constraint  $k^2 > zk'^2$  (with  $z = e^{y-Y}$ ). The function  $\Delta'$  is the non-Sudakov form factor modified to include the kinematical constraint. The correct form for  $\Delta'$  can be found by requiring that once more it can be used to exactly

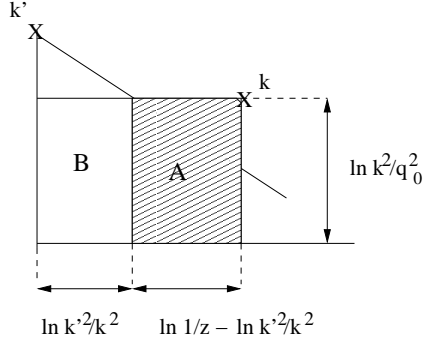


Figure 10: The phase space for the modified BFKL non-Sudakov form factor when the kinematical constraint is taken into account. Region B which was previously included is now excluded. Real  $k_{\perp}$ -conserving emissions are confined to region A.

compensate the  $k_{\perp}$ -conserving emissions which are now also modified by the kinematical constraint. The phase space for  $\Delta'$  is illustrated in Fig. 10. The region we are looking for is the shaded one, region A. Region B which was allowed before is now excluded due to the kinematical constraint. Indeed the real  $k_{\perp}$ -conserving emissions are confined to region A, since just like for CCFM, any real emission in B would create a  $t$ -channel propagator below the diagonal line, violating the kinematical constraint. It is then seen that (see also [40])

$$\begin{aligned} \Delta'(Y-y, k) &= \theta(k-k')\Delta(Y-y, k) \\ &+ \theta(k'-k) \exp(-\bar{\alpha}_s \ln(k^2/q_0^2)(\ln(k^2/k'^2) + Y-y)) \end{aligned} \quad (3.14)$$

where  $\Delta(Y-y, k)$  is the usual non-Sudakov, and the second factor is just  $\exp(-\bar{\alpha}_s A)$  (again if  $k > k'$  the kinematical constraint is automatic).

Next we inclusively sum over the  $k_{\perp}$ -conserving emissions in (3.13), canceling  $\Delta'$ . If we use the explicit constraint  $q > \min(k, k')$ , we get

$$\mathcal{A}(Y, k) = \bar{\alpha}_s \int_0^Y dy \int \frac{d^2 k'}{\pi |k-k'|^2} \theta(Y-y + \ln(k^2/k'^2)) \theta(|k-k'|^2 - \min(k^2, k'^2)) \mathcal{A}(Y, k'), \quad (3.15)$$

and this leads to an equation which is *exactly* identical to (3.9) and (3.11). We can also use the constraint  $q = \max(k, k')$  in which case we obtain (3.12). We should also mention that we could repeat the arguments in appendix D for BFKL with the kinematical constraint. In that case the region left over by the real-virtual cancellations is exactly equal to the region  $C'$  in (D.2).

#### 4. CCFM evolution with saturation boundary

The CCFM evolution, so like any other linear evolution in perturbative QCD, predicts an unlimited growth of the gluon distribution with increasing  $Y$ , thus leading to unitarity

violations in the high energy limit. This is so since the linear evolution equations miss the non-linear phenomena responsible for unitarization, which are gluon saturation and multiple scattering. It turns out, however, that the phenomenon of gluon saturation merely acts as a kind of cutoff, which limits the growth of the gluon distribution, but does not modify the mechanism responsible for this growth. This makes it possible to mimic the effects of saturation by appropriately implementing this cutoff on the linear evolution equations, without a detailed understanding of the underlying non-linear phenomena. In this section we shall motivate and describe the implementation of this cutoff — actually, an *absorptive boundary condition* —, which then will be used, in Sect. 5, within numerical simulations of the CCFM and BFKL evolutions in the presence of unitarity corrections.

#### 4.1. Unitarity and Saturation momentum

In what follows we shall explain our method for effectively implementing saturation on the example of the BFKL equation [2]. This is interesting since the corresponding non-linear generalization which obeys unitarity is also known — this is the Balitsky–Kovchegov (BK) equation [11, 12] —, and thus it can be used to test our method. The derivation of the BK equation has been recently pushed to next-to-leading order accuracy [41, 42, 43, 44], but here we shall limit ourselves to its leading-order version, which is also the accuracy of the CCFM formalism. However, this LO version will be eventually extended to include a running coupling (both for BFKL and for CCFM), since the running coupling effects modify in an essential way the high energy evolution — these are the only NLO corrections which remain important for asymptotically high energy.

The (leading-order) BK equation for the unintegrated gluon distribution reads

$$\partial_Y \mathcal{A}(Y, k) = \bar{\alpha}_s \int \frac{dk'^2}{k'^2} \left\{ \frac{k'^2 \mathcal{A}(Y, k') - k^2 \mathcal{A}(Y, k)}{|k^2 - k'^2|} + \frac{k^2 \mathcal{A}(Y, k)}{\sqrt{4k'^4 + k^4}} \right\} - \bar{\alpha}_s (\mathcal{A}(Y, k))^2. \quad (4.1)$$

The terms linear in  $\mathcal{A}(Y, k)$  in this equation represent the BFKL equation, whereas the last, quadratic, term is responsible for gluon saturation. One can roughly think about this last term as describing the recombination of two gluons into one, but this picture is quite crude: the actual non-linear phenomena responsible for gluon saturation are much more complex and should be rather viewed as the blocking of new gluon emissions by strong color fields [29]. Since this equation is non-linear, we should be more specific about the normalization of the function  $\mathcal{A}(Y, k)$ . Our conventions are such that the standard, ‘integrated’ gluon distribution is computed as

$$xg(x, Q^2) = \frac{4N_c^2}{\pi^2 \bar{\alpha}_s} \int^{Q^2} \frac{d^2k}{(2\pi)^2} \int d^2b \mathcal{A}(Y, k, b), \quad (4.2)$$

where  $b$  denotes the 2-dimensional impact parameter in the transverse space. Note that, strictly speaking, the non-linear effects are non-local in  $b$ . The simple form for the non-linear term shown in Eq. (4.1) is obtained under the further assumption that the hadron is homogeneous in  $b$  (a ‘large nucleus’). With these conventions, the *gluon occupation number* — i.e., the number of gluons of a given color per unit rapidity per unit volume in

transverse phase-space — is not exactly  $\mathcal{A}(Y, k)$ , but rather  $\mathcal{A}(Y, k)/\bar{\alpha}_s$  (up to a numerical factor).

So long as  $\mathcal{A}(Y, k) \ll 1$ , the non-linear terms in Eq. (4.1) can be neglected, and then this equation predicts the rapid, BFKL, growth of the gluon distribution, which is exponential in  $Y$ , together with diffusion in transverse space (see below). When  $\mathcal{A}(Y, k) \sim 1$  (corresponding to a physical occupation number  $\mathcal{O}(1/\bar{\alpha}_s)$ ), the non-linear effects become important and tame this growth. For a given rapidity  $Y$ , this happens at a specific value of the transverse momentum  $k = Q_s(Y)$ , called the *saturation momentum*, which grows rapidly with  $Y$  (see below). One can show that at low momenta  $k \lesssim Q_s(Y)$ , the occupation number essentially *saturates*, in the sense that it shows only a very slow increase<sup>7</sup> with  $Y$ :  $\mathcal{A}(Y, k) \simeq \ln[Q_s(Y)/k]$ . Hence, for a given  $Y$ , the gluon distribution  $\mathcal{A}(Y, k)$  produced by the BK equation looks like a *front*, which interpolates between the dilute ( $\mathcal{A}(Y, k) \ll 1$ ) BFKL tail<sup>8</sup> at high transverse momenta  $k \gg Q_s(Y)$  and a saturation region at low transverse momenta  $k \lesssim Q_s(Y)$ , where  $\mathcal{A}(Y, k) \sim \ln[Q_s(Y)/k]$ . The transition between these two regions occurs around  $k = Q_s(Y)$ , where  $\mathcal{A}(Y, k) \sim 1$ . With increasing  $Y$ , this transition value  $Q_s(Y)$  is rapidly increasing, i.e., the front moves up to higher values of  $k$ .

What is remarkable about this dynamics is that the progression of the front with increasing energy and also its shape at high  $k$  are fully determined by the BFKL evolution of the dilute tail at  $k \gg Q_s(Y)$ , and thus can be inferred from the linear, BFKL, equation alone. One says that the saturation front is “pulled by its tail”. This property is central to our analysis: it implies that some essential features of the dynamics in the presence of saturation, like the energy dependence of the saturation momentum, can be studied without a detailed knowledge of the non-linear effects responsible for saturation. Hence, a similar study can be performed on the basis of other equations, so like CCFM, whose non-linear generalizations are not known.

The pulled-front property is highly non-trivial — there are many examples of non-linear equations which develop a *pushed front*, i.e., a front whose progression is driven by the growth and accumulation of ‘matter’ behind the front [45] — and so far it has not been rigorously demonstrated for the general case in QCD. In the case of a *fixed coupling* and for *sufficiently high energy*, this property follows from the identification [8] between the asymptotic form of the BK equation at high energy<sup>9</sup> and the FKPP equation (from Fisher Kolmogorov, Petrovsky, and Piskunov) of statistical physics. (The FKPP equation describes a ‘reaction-diffusion process’ in the mean field approximation corresponding to very large occupation numbers at saturation; see e.g. the review paper [45].) However, this identification does not extend to a *running* coupling, and it was in fact shown [10] that the high-energy evolution with running coupling is not in the same universality class as the reaction-diffusion. Yet, the pulled-front property appears to hold for that case

---

<sup>7</sup>The dependence of  $Q_s(Y)$  upon  $Y$  is such that the physical occupation number at  $k \lesssim Q_s(Y)$  grows linearly with  $Y$ ; that is, what saturates is the *rate* for gluon emission [29].

<sup>8</sup>In particular, for extremely high  $k \gg Q_s(Y)$ , the BFKL distribution approaches the bremsstrahlung spectrum,  $\mathcal{A}(Y, k) \sim 1/k^2$ , whereas at moderate  $k$  this is modified by the BFKL ‘anomalous dimension’.

<sup>9</sup>This is obtained via the gradient expansion of the non-locality in Eq. (4.1) to second order in  $\partial/\partial\rho$ , with  $\rho = \ln k^2$  (‘diffusion approximation’).



too, and also for relatively small rapidities (*i.e.*, for the early stages of the evolution), as most convincingly demonstrated so far by the numerical simulations in Ref. [1], where the solutions to the BK equation with running coupling have been systematically compared to those of the BFKL equation supplemented with a saturation boundary condition.

In order to gain some analytic insight into the role and the form of this boundary condition, it is useful to briefly review the computation of the saturation momentum from the BFKL equation [6, 7] — in the fixed coupling case, for simplicity (the corresponding developments for the case of a running coupling can be found in Refs. [7, 15]). We start with the Mellin representation of the BFKL solution, that is

$$\mathcal{A}(Y, k) = \int_C \frac{d\gamma}{2\pi i} e^{\bar{\alpha}_s \chi(\gamma) Y - (1-\gamma)\rho} \tilde{\mathcal{A}}(\gamma), \quad (4.3)$$

where  $\rho \equiv \ln(k^2/Q_0^2)$  with  $Q_0$  an arbitrary reference scale,  $\tilde{\mathcal{A}}(\gamma)$  is the initial condition at  $Y = 0$ , and  $\chi(\gamma)$  is the BFKL characteristic function, *i.e.* the eigenvalue of the BFKL kernel in Mellin space:

$$\chi(\gamma) = 2\psi(1) - \psi(\gamma) - \psi(1 - \gamma), \quad \psi(\gamma) \equiv d \ln \Gamma(\gamma) / d\gamma. \quad (4.4)$$

The integration contour  $C$  runs parallel to the imaginary axis with  $0 < \text{Re}(\gamma) < 1$ . For real values of  $\gamma$  in between 0 and 1 (the relevant range for computing the saddle point; see below), the function  $\chi(\gamma)$  is displayed in Fig. 11.

Eq. (4.3) is expected to be correct so long as  $\mathcal{A}(Y, k) \ll 1$ , *i.e.* for high enough momenta  $k \gg Q_s(Y)$ . Here we shall assume that this expression can be also used to approach the saturation line ‘from the above’ (*i.e.* from momenta  $k$  larger than  $Q_s$ ), and hence to approximately determine the latter from the condition that  $\mathcal{A}(Y, k) \sim 1$  when  $k = Q_s(Y)$ . To that aim, we shall also rely on the saddle point approximation, which is appropriate for high enough  $Y$  — namely, such that  $\bar{\alpha}_s Y \gg 1$ . By combining the saddle point condition

$$\bar{\alpha}_s Y \chi'(\gamma_s) = -\rho_s, \quad (4.5)$$

with the condition that  $\mathcal{A}(Y, k) \sim 1$  along the saturation line:

$$\bar{\alpha}_s Y \chi(\gamma_s) - (1 - \gamma_s)\rho_s = 0, \quad (4.6)$$

one obtains  $\gamma_s$  and the saturation line  $\rho_s(Y) \equiv \ln[Q_s^2(Y)/k_0^2]$  as follows [6]

$$\begin{aligned} \frac{\chi'(\gamma_s)}{\chi(\gamma_s)} &= -\frac{1}{1 - \gamma_s} \implies \gamma_s \approx 0.372, \\ \rho_s(Y) &\simeq \lambda_s Y \quad \text{with} \quad \lambda_s \equiv \bar{\alpha}_s \frac{\chi(\gamma_s)}{1 - \gamma_s} \approx 4.883 \bar{\alpha}_s. \end{aligned} \quad (4.7)$$

A geometrical interpretation of the above equation for  $\gamma_s$  is shown in Fig. 11.

For  $\rho$  larger than  $\rho_s$ , but not *much* larger, one can estimate the gluon distribution by expanding the integrand in Eq. (4.3) around  $\gamma_s$  : writing  $\gamma = \gamma_s - i\nu$ , and expanding to second order in  $\nu$ , one finds

$$\bar{\alpha}_s Y \chi(\gamma) - (1 - \gamma)\rho \simeq -(1 - \gamma_s)(\rho - \rho_s) - i\nu(\rho - \rho_s) - D_s Y \nu^2, \quad (4.8)$$

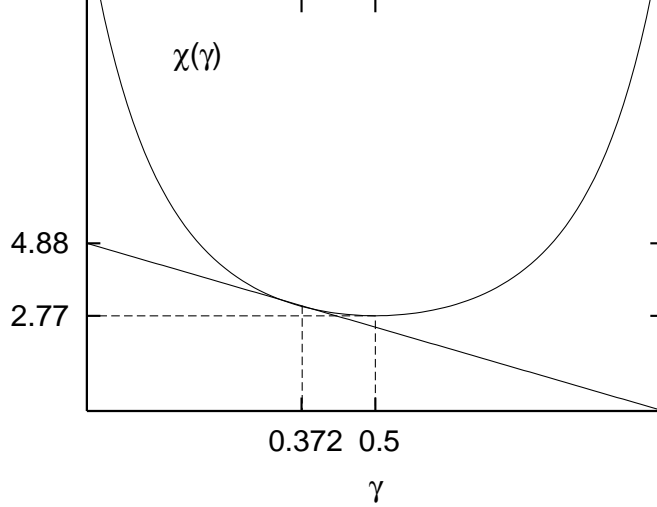


Figure 11: The BFKL eigenvalue  $\chi(\gamma)$  and the graphical solution to the saturation problem. The value  $\gamma_s = 0.327$  corresponds to the saturation saddle point and the value  $\chi(\gamma_s)/\gamma_s = 4.88$  determines the asymptotic energy dependence of the saturation momentum (for comparison, the “hard pomeron” saddle point  $\gamma_{\mathbb{P}} = 1/2$  and its intercept  $\omega_{\mathbb{P}} = 4 \ln 2 = 2.77$  are shown).

where  $D_s = \bar{\alpha}_s \chi''(\gamma_s)/2 \approx 24.26 \bar{\alpha}_s$ . This expansion is valid so long as  $1 < \rho - \rho_s \ll D_s Y$ . After also performing the Gaussian integration over  $\nu$ , one finds [6]

$$\mathcal{A}(Y, k) \simeq \frac{1}{\sqrt{\pi D_s Y}} \left( \frac{Q_s^2}{k^2} \right)^{1-\gamma_s} \exp \left\{ -\frac{\ln^2(k^2/Q_s^2)}{4D_s Y} \right\}, \quad (4.9)$$

with  $Q_s^2(Y) = Q_0^2 e^{\lambda_s Y}$ . Eq. (4.9) exhibits a power-like spectrum in  $k$  with anomalous dimension (*i.e.*, deviation from the bremsstrahlung spectrum)  $\gamma_s$ , which is further modified by BFKL diffusion (the last factor, which is a Gaussian in  $\ln(k^2/Q_s^2) = \rho - \rho_s$ ).

Although obtained solely from the linear, BFKL, equation, the above results for the behaviour near saturation are essentially correct: they coincide with the respective predictions of the BK equation for asymptotically high energy. It turns out that one can do even better: still without resorting on the actual non-linear Eq. (4.1), one can also determine the sub-asymptotic behaviour of  $Q_s^2(Y)$  at large  $Y$ , and refine the approach of  $\mathcal{A}(Y, k)$  towards saturation. The main observation, which lies also at the heart of the subsequent developments in this work, is that the saturation region acts like an *absorptive boundary* [7], which not only tames the growth of the gluon distribution, but also prevents the BFKL diffusion towards lower momenta  $k \lesssim Q_s(Y)$ .

After also implementing this absorptive boundary, in a way to be shortly specified, the previous formulæ are modified as follows [7]: the gluon distribution becomes

$$\mathcal{A}(Y, \rho) \sim (\rho - \rho_s + \delta) e^{-(1-\gamma_s)(\rho-\rho_s)} \exp \left\{ -\frac{(\rho - \rho_s)^2}{2D_s Y} \right\}, \quad (4.10)$$

where  $\delta \sim 1$  is some unknown constant and  $\rho_s(Y)$  is now under control up to next-to-leading order in the asymptotic expansion at high-energy:

$$\rho_s(Y) \simeq \lambda_s Y - \frac{3}{2\gamma_s} \ln Y. \quad (4.11)$$

These results coincide indeed with the corresponding predictions of the non-linear, BK, equation, as deduced via the correspondence with the FKPP equation [8]. Notice in particular the property of *geometric scaling* [6, 7]: within the region  $\rho - \rho_s \ll \sqrt{2D_s Y}$ , whose width is increasing with  $Y$ , the Gaussian factor can be ignored in Eq. (4.10), and then this expression reduces to a function of  $\rho - \rho_s(Y)$  alone, *i.e.* of the scaling variable  $Q^2/Q_s^2(Y)$ . This property provides a natural explanation for an important regularity observed in the HERA data for DIS at small- $x$  [16].

The success of the absorptive boundary method for the BFKL evolution makes it compelling to try and use it as a systematic method for enforcing saturation within an arbitrary linear evolution, so like CCFM. Let us now explain in detail our practical implementation of the absorptive boundary, as it will be used within numerical simulations. We first introduce a line of constant gluon occupancy  $\rho = \rho_c(Y)$  via the condition

$$\mathcal{A}(Y, \rho = \rho_c(Y)) = c, \quad (4.12)$$

where the number  $c$  is smaller than one, but not *much* smaller. The saturation line  $\rho_s(Y)$  would correspond to  $c \sim 1$ , so clearly  $\rho_s(Y)$  is smaller than  $\rho_c(Y)$ , but relatively close to it. (For the BK evolution with fixed coupling, these two lines would be parallel lines, with slope  $\lambda_s$ , separated from each other by  $\rho_c(Y) - \rho_s(Y) \sim \ln(1/c)$ .) For  $\rho < \rho_c(Y)$  and sufficiently high energy, the solution  $\mathcal{A}_{\text{BFKL}}(Y, \rho)$  to the BFKL equation would become larger than one — in fact, arbitrarily large. If this equation is to be solved numerically, one may think about enforcing saturation by hand, in the following way: at each step in  $Y$ , one first identifies the corresponding point  $\rho_c(Y)$  from the condition (4.12), and then one requires  $\mathcal{A}(Y, \rho)$  to remain finite and of  $\mathcal{O}(1)$  for any  $\rho$  sufficiently far below  $\rho_c(Y)$  — say, for  $\rho \leq \rho_c(Y) - \Delta$  with  $\Delta \simeq \ln(1/c)$ . When decreasing  $\rho$  below  $\rho_c(Y)$ , the solution  $\mathcal{A}(Y, \rho)$  will typically start by rising, then reach a maximum of  $\mathcal{O}(1)$  and eventually decrease to zero. We shall conventionally identify the saturation scale  $\rho_s(Y)$  with the position of this maximum. In this procedure, the numbers  $c$  and  $\Delta$  are to be viewed as free parameters, which are however correlated with each other, since  $\Delta \sim \ln(1/c)$ .

By construction, the value of  $\mathcal{A}(Y, \rho)$  behind the saturation front is not under control, as this is fixed by hand at a constant value. In practice we shall choose this constant value to be zero:  $\mathcal{A}(Y, \rho) = 0$  for  $\rho \leq \rho_c(Y) - \Delta$  (but other values of  $\mathcal{O}(1)$  will be also used, to test the sensitivity of the method to this particular choice). Thus, clearly, our procedure cannot be used for those physical problems which are sensitive to the details of the saturation region, like deep inelastic scattering at low  $Q^2 \lesssim Q_s^2(Y)$ , or particle production at low transverse momenta. On the other hand, this procedure accurately describes the dynamics of the front, in that it provides the same results as the non-linear BK equation for the energy dependence of the saturation momentum and for the gluon distribution  $\mathcal{A}(Y, k)$  at momenta  $k > Q_s(Y)$ , for both fixed and running coupling, and for all values of  $Y$ .

Let us illustrate the efficiency of this method with a few numerical results for the case of a running coupling. We include running coupling by pulling the  $\bar{\alpha}_s$  factor inside the  $k'$ -integral in Eq. (4.1) and using the one-loop expression for the running coupling with scale  $Q^2 = \max(k^2, k'^2)$  and  $\Lambda_{\text{QCD}} = 200$  MeV. This simple prescription is in agreement with the recently constructed running-coupling version of the BK equation [41, 42]. To avoid the infrared divergence of the coupling at  $Q^2 = \Lambda_{\text{QCD}}^2$ , we shall replace  $\alpha_s(Q^2) \rightarrow \alpha_s(Q^2 + \mu^2)$  for some parameter  $\mu$ . Our default choice will be  $\mu^2 = 0.5$  GeV<sup>2</sup>, but we shall study the sensitivity of our results to variations in  $\mu$ . Our initial condition  $\mathcal{A}(Y = 0, k)$  is given by the bremsstrahlung spectrum for  $k > 1$  GeV (with maximal height  $\mathcal{A} = 0.5$ ) and it vanishes for  $k < 1$  GeV.

The pure BFKL evolution with running coupling is known to be infrared unstable: the rise of the gluon distribution is much faster at small values of  $k$  (where the coupling is larger) and, besides, this rapid accumulation of gluons in the infrared is also feeding the growth at higher  $k$ . Therefore the linear evolution behaves quite differently compared to the non-linear one, even at high  $k$ . To illustrate that, we have also included in Fig. 12 the results of the strict BFKL evolution, which indeed show a much faster progression towards high  $k$  as compared to the BK equation. On the other hand, one observes a perfect matching between the saturation fronts provided by BK and, respectively, BFKL with saturation boundary. This shows that the front remains of the pulled type even with running coupling and at the same time demonstrates the success of our method for effectively implementing saturation. We also note that in the corresponding figures in [1], the values  $c = 0.1$  and  $\Delta = 5.0$  were used instead of  $c = 0.4$  and  $\Delta = 2.0$ , thus showing that the results do not depend on the specific values of these parameters (as long as they are correlated as  $\Delta \sim \ln(1/c)$ ).

In particular, the infrared problem is cured by saturation: the saturation scale effectively acts as an infrared cutoff, which becomes ‘hard’ ( $Q_s^2(Y) \gg \Lambda_{\text{QCD}}^2$ ) for sufficiently high energy. To better illustrate this, we exhibit in Fig. 13 results obtained for different values of the IR cutoff  $\mu^2$  inserted in the running coupling. Unlike the pure BFKL results (left figure), which are extremely sensitive to a change in  $\mu$ , the results corresponding to the saturation boundary condition (right figure) show no sensitivity whatsoever.

From the curves in Fig. 12, it is also possible to extract the  $Y$ -dependence of the saturation momentum  $\rho_s(Y)$  for running coupling. We find that the squared-root law  $\rho_s \simeq \lambda_r \sqrt{Y}$  predicted by the theory [6, 7, 15] for asymptotically high energies provides a good fit to our numerical results for  $Y \geq 10$ , with a fitted value  $\lambda_r \simeq 2.9$  which agrees reasonably well with the (asymptotic) theoretical expectation<sup>10</sup>  $\lambda_r \simeq 3.2$ .

Now, from the phenomenological point of view, we are more interested in values of  $Y$  which are not that large, say  $Y \leq 14$  (corresponding to  $x \gtrsim 10^{-6}$ ), as relevant for forward jet production at LHC. With that in mind, we also show in Fig. 12 (right) the results for lower values of  $Y$ , between 6 and 12 units; one can thus see that the absorptive boundary

---

<sup>10</sup>For asymptotically large  $Y$ , the running-coupling BFKL evolution yields [6, 7] :  $\rho_s(Y) \simeq \sqrt{2\lambda_0 b_0 Y}$  where  $\lambda_0 \simeq 4.88$  is the same number as in Eq. (4.11) and  $b_0 \equiv 12N_c/(11N_c - 2N_f)$  is the coefficient in the one-loop running coupling:  $\bar{\alpha}(Q^2) = b_0/\ln(Q^2/\Lambda_{\text{QCD}}^2)$ . In our simulations, we use  $N_f = 0$ , hence we expect  $\lambda_r \equiv \sqrt{2\lambda_0 b_0} \simeq 3.26$ , which is indeed consistent with the fit to the curves in Fig. 12.

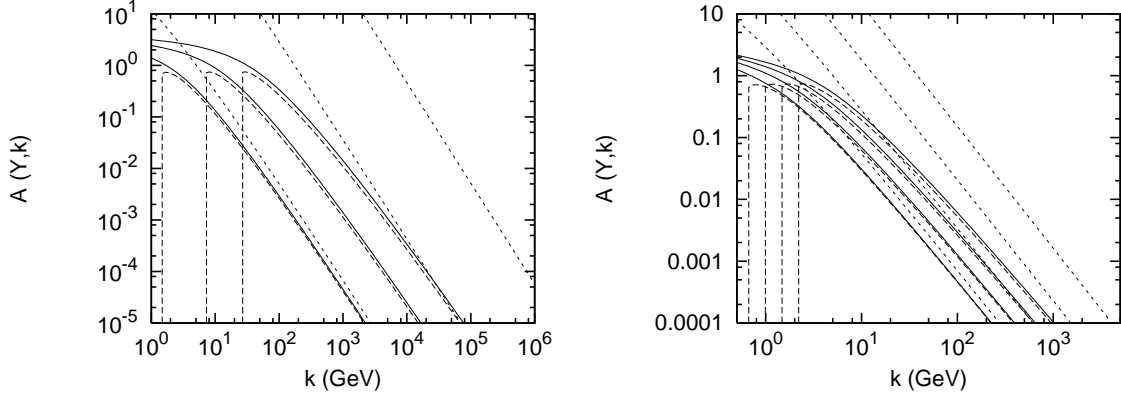


Figure 12: The running coupling results for: BK (solid curves), BFKL with absorptive boundary (long dashed curves) and pure BFKL (short dashed curves) for (left)  $Y = 10, 20, 30$  and  $40$ , and (right)  $Y = 6, 8, 10$  and  $12$ . For the absorptive boundary we used  $c = 0.4$  and  $\Delta = 2.0$ .

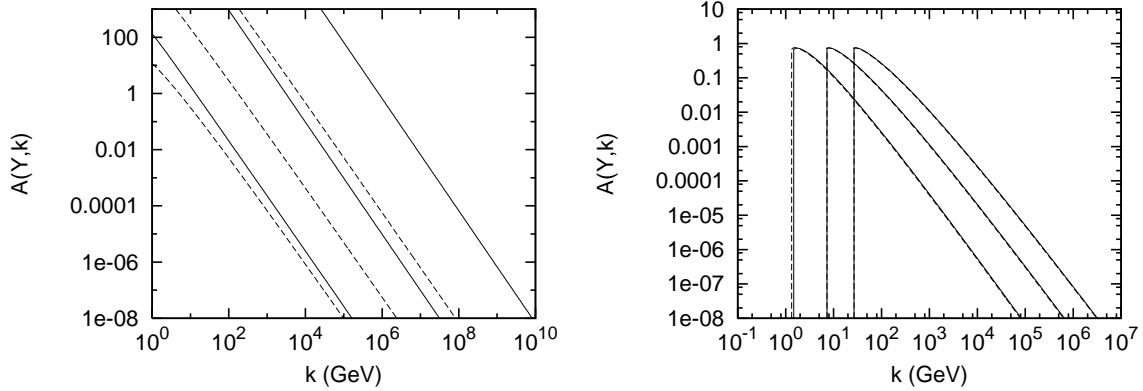


Figure 13: Testing the sensitivity of the BFKL evolution to the IR cutoff  $\mu$ . Left: The pure BFKL evolution with  $\mu^2 = 0.5 \text{ GeV}^2$  (solid lines) and  $\mu^2 = 2.0 \text{ GeV}^2$  (dashed lines), for  $Y = 10, 20$  and  $30$ . Right: The BFKL evolution with absorptive boundary for  $\mu^2 = 0.5 \text{ GeV}^2$  (solid lines),  $\mu^2 = 2.0 \text{ GeV}^2$  (dashed lines) and for the same values for  $Y$  as before.

method works equally well also for such lower rapidities.

#### 4.2. CCFM evolution in presence of saturation: analytic results

Within numerical simulations, it is straightforward to implement the saturation boundary condition in any of the previous versions of the CCFM equation: the complete, integral, equation (3.1), or one of its simpler, differential, equations deduced in Sect. 3.3. Given the approximations made in deriving the latter, it is clear that the corresponding results will not be exactly the same. In particular, the saturation momentum deduced from the full CCFM equation (3.1) will also depend upon the maximal angle variable  $\bar{\xi}$  introduced by the kinematics of the external scattering; in the case of DIS, this means that  $Q_s$  will depend upon the virtuality scale  $Q^2$  at which one measures the structure functions. It would be very interesting to study this dependence, and also the energy dependence of

$Q_s$ , by numerically solving the integral equation (3.1) in the presence of saturation. This could be done via Monte Carlo simulations (e.g., by correspondingly extending the CASCADE event generator [13]), which would also allow one to study the effects of saturation on the structure of the final state. Such numerical calculations would be however tedious in practice, and it would be very difficult to reach high values of  $Y$  in this way. Our interest here is mostly conceptual: we would like to understand how saturation modifies the CCFM evolution, and how the respective predictions compare to those based on the BFKL evolution (with saturation once again). To that aim, we shall focus on the differential versions of the CCFM equation, for which we shall present some analytic estimates in this section, and then a systematic numerical study in Sect. 5.

The analytic study is based on the Mellin transform, as already introduced in Eq. (4.3). In what follows we will generically denote the kernel eigenfunction (the quantity denoted as  $\bar{\alpha}_s \chi(\gamma)$  in (4.3)) as  $\omega(\bar{\alpha}_s, \gamma)$ , keeping the notation  $\chi(\gamma)$  only for the BFKL eigenfunction (4.4). In the case of Eq. (3.12), the function  $\omega$  can be analytically computed, while for Eq. (3.11) it must be constructed numerically. Namely, for Eq. (3.12), we get

$$\omega = \bar{\alpha}_s \left( \frac{1}{\gamma} + \frac{1}{1 - \gamma + \omega} \right), \quad (4.13)$$

which is easily solved to give

$$\omega = -\frac{1}{2} \left( 1 - \gamma - \frac{\bar{\alpha}_s}{\gamma} \right) + \sqrt{\frac{1}{4} \left( 1 - \gamma - \frac{\bar{\alpha}_s}{\gamma} \right)^2 + \frac{\bar{\alpha}_s}{\gamma}}. \quad (4.14)$$

For  $\bar{\alpha}_s \rightarrow 0$  this expression reduces to

$$\omega = \bar{\alpha}_s \left( \frac{1}{\gamma} + \frac{1}{1 - \gamma} \right) \quad (4.15)$$

where  $1/\gamma$  is recognized as the collinear piece (the one which dominates when  $k \gg k'$ ), while  $1/(1 - \gamma)$  is the anti-collinear one ( $k' \gg k$ ). The high-energy saddle point coincides with the BFKL one,  $\gamma = 1/2$ , but the intercept is given by 4, instead of 2.77 for BFKL. The saturation saddle point,  $\gamma_s$ , is found according to Eq. (4.7) which now becomes

$$\omega'(\gamma_s) = \frac{\omega(\gamma_s)}{1 - \gamma_s}. \quad (4.16)$$

This gives  $\gamma_s = 1/3 \simeq 0.33$ , which is quite close to the respective BFKL value  $\gamma_s \simeq 0.37$ . The saturation exponent  $\lambda_s$  controlling the growth of the saturation momentum is again obtained from (4.7) which in this case gives 6.75, and thus is larger than the respective BFKL value 4.88.

Although the eigenfunction (4.15) gives a too high intercept and a too large speed of the saturation front, it is well known that it approximates the general shape for the BFKL eigenfunction,  $\chi(\gamma)$ , very well. (This explains why the respective saturation saddle points are so close to each other.) In fact if one just subtracts from (4.15) the difference of the two intercepts,  $4 - 4 \ln 2$ , then an almost perfect approximation of  $\chi(\gamma)$  is obtained. Note

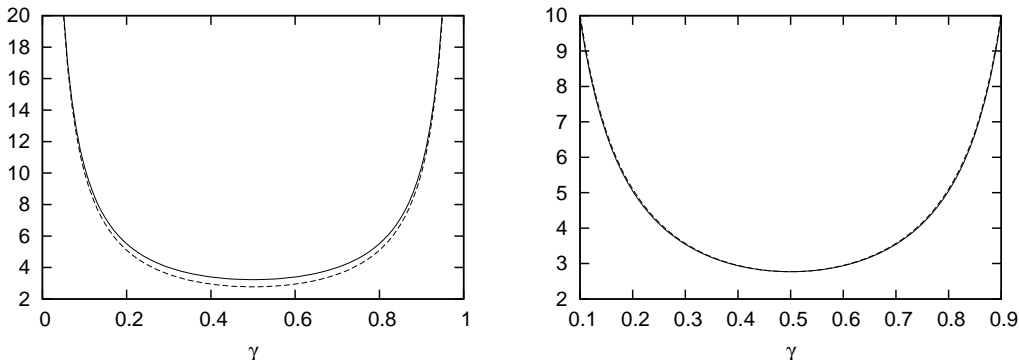


Figure 14: *Left: The Mellin space eigenfunction of the asymptotic approximation of Eq. (3.11) (solid line) compared to the BFKL eigenfunction  $\chi(\gamma)$  (dashed line). Right: The same as in left but with a constant 0.45 subtracted from the solid line.*

that a constant shift in the eigenfunction corresponds in momentum space to the inclusion of a local term  $\propto \mathcal{A}(Y, k)$  in the right-hand side of the differential equation.

For Eq. (3.11), we write  $\omega = \bar{\alpha}_s \tilde{\chi}(\gamma, \omega)$ , where  $\tilde{\chi}$  can be numerically constructed. In the weak coupling limit ( $\bar{\alpha}_s \rightarrow 0$ ) we have

$$\omega = \bar{\alpha}_s \tilde{\chi}(\gamma) = \bar{\alpha}_s \int_0^1 dt \frac{h(t)}{1-t} (t^{-\gamma} + t^{-(1-\gamma)}). \quad (4.17)$$

To find the behaviour at the endpoints,  $\gamma = 0$  and  $\gamma = 1$ , we concentrate on the region  $t \approx 0$  and use that  $h(t) = 1$  for  $t < 1/4$ . This yields

$$\begin{aligned} & \int_0^{1/4} dt \frac{1}{1-t} (t^{-\gamma} + t^{-(1-\gamma)}) = \\ & = \frac{(1/4)^{1-\gamma}}{1-\gamma} F(1-\gamma, 1, 2-\gamma, 1/4) + \frac{(1/4)^\gamma}{\gamma} F(\gamma, 1, 1+\gamma, 1/4), \end{aligned} \quad (4.18)$$

where  $F$  is the hypergeometric function. Since at the endpoints we have  $F \rightarrow 1$  for each term, we find the same endpoint behaviour as (4.15), and hence as in BFKL. For the complete interval we plot  $\tilde{\chi}$ , together with  $\chi$ , in Fig. 14. We see that the minimum of  $\tilde{\chi}$ , *i.e.* the intercept, is a bit above the BFKL one — this is numerically found as 3.23 —, and therefore so is also the respective saturation exponent, found as  $\lambda_s \simeq 5.56$ . On the other hand, the shape of the eigenfunction is again very similar to the BFKL one: in the right figure 14 we have subtracted the difference between the two intercepts, *i.e.* 0.45, from  $\tilde{\chi}$ , and then the two curves almost coincide. So, no surprisingly, the saturation anomalous dimension  $\gamma_s \simeq 0.35$  is close to the respective BFKL value. As previously noted, such a constant subtraction is tantamount to a contribution proportional to  $\mathcal{A}(Y, k)$  in the differential equation, which in turn can be associated with additional virtual corrections. In appendix D we will see that such virtual terms naturally appears in Eq. (3.11) when the real-virtual cancellations are treated with a better accuracy.

Before leaving this section, we demonstrate the behaviour of the eigenfunctions for any  $\bar{\alpha}_s$ . For finite  $\bar{\alpha}_s$ , the anti-collinear pole is screened by  $\omega$  appearing in the r.h.s. of (4.13)

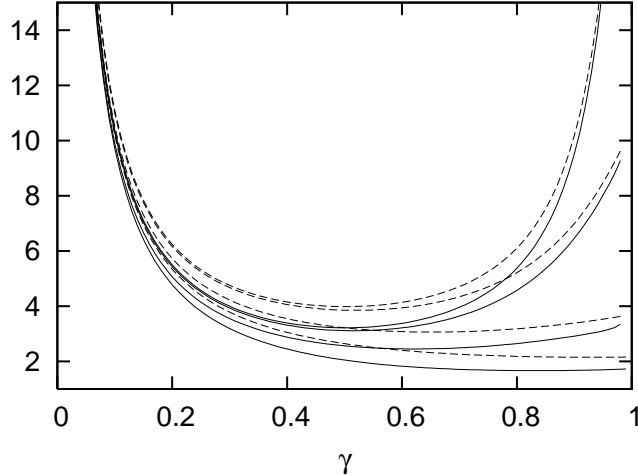


Figure 15: The eigenfunctions  $\omega/\bar{\alpha}_s$  for equations (3.11) (solid line) and (3.12) (dashed line), for 4 values of the coupling (from up to down) :  $\bar{\alpha}_s = 0.001, 0.01, 0.1$ , and  $0.4$ . The very small values of  $\bar{\alpha}_s$  are included to illustrate the emergence of the anti-collinear pole at  $\gamma = 1$  in the limit  $\bar{\alpha}_s \rightarrow 0$ .

and the corresponding equation for (3.11). The pole appearing in (4.15) is really valid only when  $\bar{\alpha}_s = 0$ . In Fig. 15 we plot the eigenfunctions,  $\omega/\bar{\alpha}_s$ , for (3.11) and (3.12) for various values of  $\bar{\alpha}_s$ . The figure clearly demonstrates the emergence of the anti-collinear pole as  $\bar{\alpha}_s \rightarrow 0$ .

## 5. Numerical results

In this section, we shall present numerical solutions for the two differential versions of the CCFM evolution derived in section 3.3, namely Eqs. (3.11) and (3.12), and also for the BFKL equation including the kinematical constraint, cf. Eqs. (3.13) and (3.14). We shall mostly focus on the unitarity-preserving versions of these equations, as obtained after implementing the saturation boundary described in Sect. 4.1. But before doing that, it is also instructive to compare the respective linear evolutions, in order to illustrate the significant differences between them (in agreement with the discussion in Sect. 4.1), and thus emphasize the ambiguity in our current understanding of high-energy evolution within perturbative QCD. Remarkably, it will turn out that this ambiguity is drastically reduced after including the saturation effects in the form of the absorptive boundary. Namely, the main conclusion that will emerge from our analysis is that all the equations under consideration — the CCFM equations (3.11) and (3.12), and the BFKL equation with and without the kinematical constraint —, which differ significantly from each other in the linear regime, lead nevertheless to very similar predictions for the energy dependence of the saturation momentum after adding the saturation boundary condition and with a running coupling. Note that the inclusion of the running coupling is essential in that sense: with a fixed coupling, important differences persist even after including saturation, as it should be expected from the discussion in Sect. 4.1.



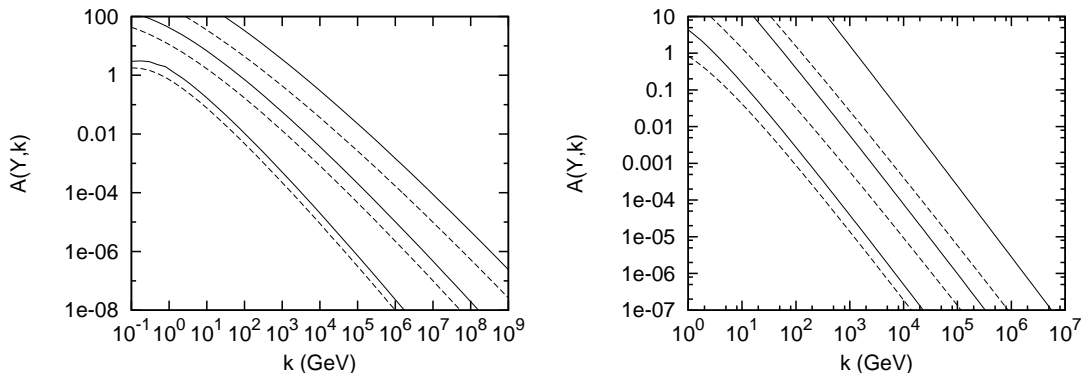


Figure 16: *The solutions to (3.11) (solid lines), and the BFKL equation including the kinematical constraint (5.1) (dashed lines) for  $Y = 10, 20$  and  $30$ . Left: fixed coupling  $\alpha_s = 0.2$ . Right: running coupling.*

For the purposes of the numerics, it is convenient to rewrite Eq. (3.13) in differential form and perform the azimuthal integration; this yields:

$$\begin{aligned} \partial_Y \mathcal{A}(Y, k) &= \bar{\alpha}_s \int dk'^2 \left( \frac{\theta(k - k') \mathcal{A}(Y, k') + \theta(k' - k) \theta(Y - \ln(k'^2/k^2)) \mathcal{A}(Y - \ln(k'^2/k^2), k')}{|k^2 - k'^2|} \right. \\ &\quad \left. - \frac{k^2}{k'^2} \left( \frac{\mathcal{A}(Y, k)}{|k^2 - k'^2|} - \frac{\mathcal{A}(Y, k)}{\sqrt{4k'^4 + k^4}} \right) \right). \end{aligned} \quad (5.1)$$

In Fig. 16 we show the solutions to the linear equations (3.11) and (5.1). As expected from the discussion in Sect. 4.1, one sees that the CCFM solution is somewhat faster. The difference is more pronounced for a running coupling, due to the infrared instability of the linear evolution. But even with a running coupling, the present equations (5.1) and (3.11), which include the kinematical constraint, predict a growth for the gluon distribution which is strongly reduced as compared to the strict BFKL equation (without kinematical constraint). This was shown in Ref. [1] where the solutions of (3.11) have been compared to the solutions of the pure BFKL equation.

Let us now perform a similar comparison after adding the saturation boundary. (Unless otherwise stated, we use the values  $c = 0.1$  and  $\Delta = 5.0$  for all calculations including the saturation boundary. A different set of values will be used later on, to illustrate the robustness of our results.) For the same  $Y$  values as in Fig. 16, we compare in Fig. 17 the respective predictions of Eqs. (3.11) and (5.1) for both fixed and running coupling. To make the comparison between the solutions easier, we have scaled the solutions to (5.1) so that the solutions more or less coincide at  $Y = 10$ . For the fixed coupling case (left plot) the scaling factor is 3.9 while for the running coupling case (right plot) it is 3.6. The difference between the fixed and the running coupling cases is striking. For fixed coupling, the saturation front generated by (3.11) is seen to progress significantly faster than the one generated by (5.1). For the running coupling case on the other hand, it is clear that the respective fronts progress with similar speeds. Thus in this case the two equations have similar predictions for the energy dependence of the saturation momentum, so that the entire difference between them can (almost) be removed by either a rescaling of the

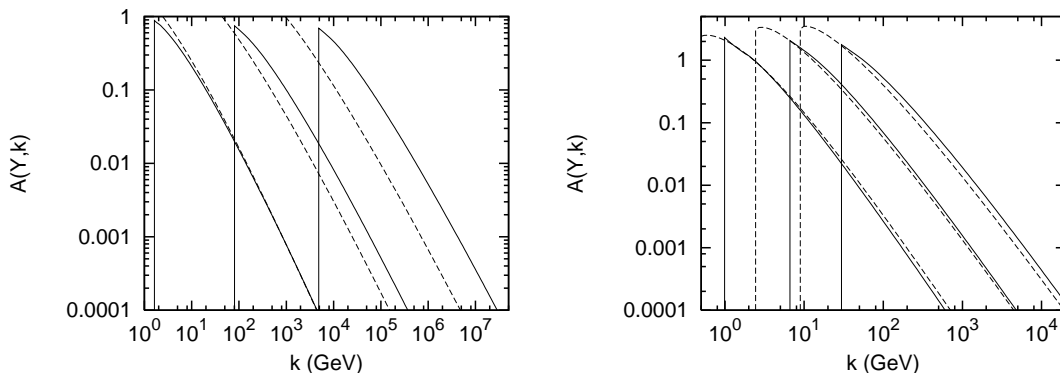


Figure 17: *The solutions to equations (3.11) (solid lines) and (5.1) (dashed lines) including the saturation boundary, for  $Y = 10, 20, 30$ . The solutions to (5.1) have been scaled so that the solutions match at  $Y = 10$ . Left: fixed coupling  $\alpha_s = 0.2$ . Right: running coupling.*

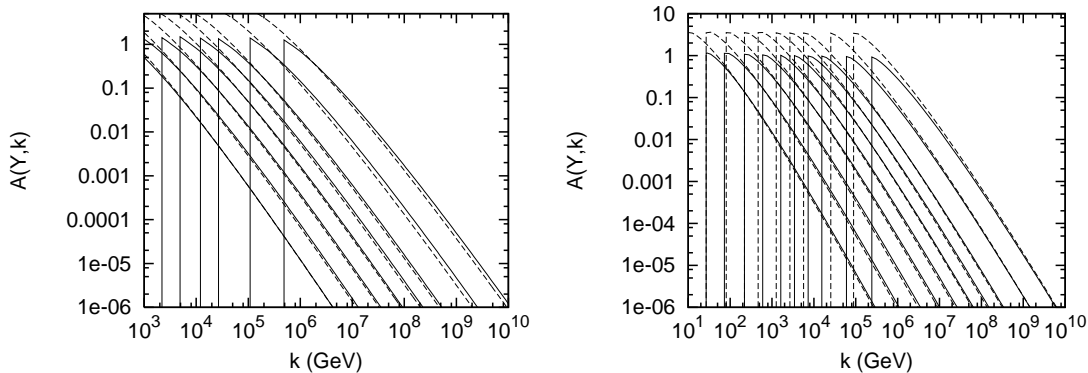


Figure 18: *Solutions to (3.11), (5.1) and BFKL including the saturation boundary for asymptotic  $Y$  between 50 and 140 units, and for a running coupling. Left: (3.11) (dashed lines) and (5.1) (solid lines). The solution to (5.1) has been scaled by a factor 6.5. Right: BFKL (dashed lines) and (5.1) (solid lines). The solution to (5.1) has been scaled by a factor 4.*

saturation momentum  $Q_s$ , or as in the figure, a rescaling of  $\mathcal{A}$ . This is clearly not the case for a fixed coupling. Note also that the difference in the fixed coupling case is visibly large even though the scale of the figure is much larger than corresponding running coupling plot.

In Fig. 18 (left) we show the respective results for the running coupling case for much higher values of  $Y$ . Also, in the right figure there, we compare the absorptive boundary results for Eq. (5.1) and, respectively, the standard BFKL equation without the kinematical constraint. One clearly sees now that, as anticipated, all the equations under consideration give approximately the same speed for the saturation front, at least up to  $Y = 140$ . To make this similarity more manifest, we have rescaled the gluon distributions by appropriate factors, in such a way to superpose the different sets of fronts. These factors account for the difference in the overall normalization of the saturation momenta provided by the different equations.

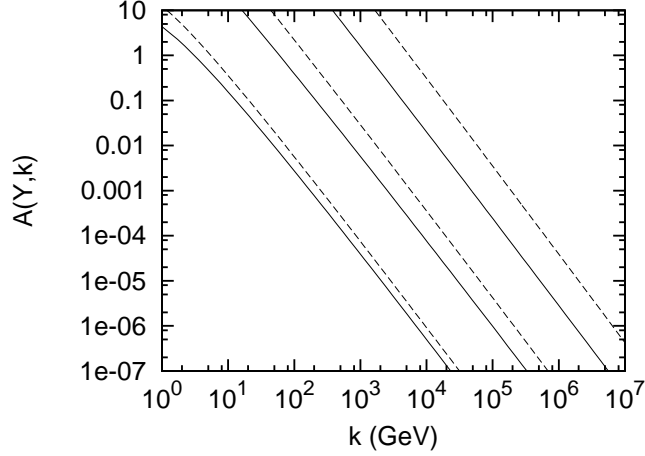


Figure 19: The solutions to equations (3.11) (solid lines) and (3.12) (dashed lines) in the linear case with a running coupling for  $Y = 10, 20$  and  $30$ .

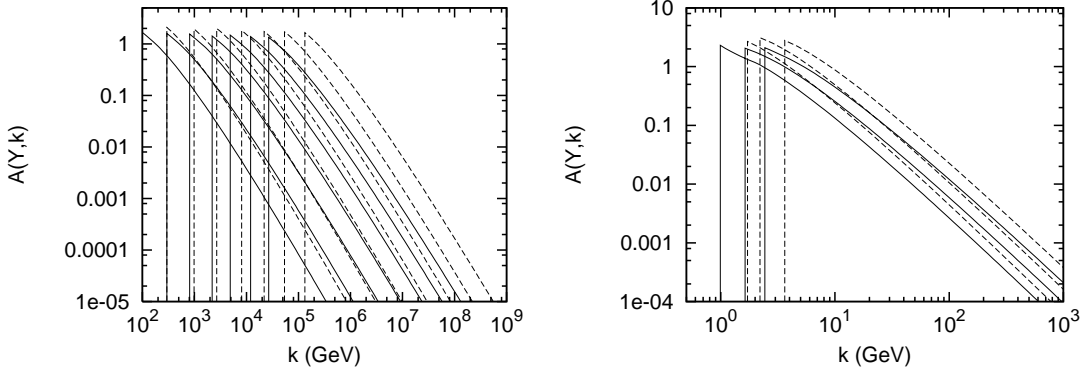


Figure 20: The solutions to equations (3.11) (solid lines) and (3.12) (dashed lines) including the saturation boundary and for a running coupling for Left: Very high  $Y$  between  $40$  and  $100$ . Right: The phenomenologically relevant values of  $Y = 10, 12, 14$ .

We have also checked that the energy dependence of the saturation momentum is consistent with the form expected at running coupling, *i.e.*,  $Q_s^2 = Q_0^2 e^{\lambda_r \sqrt{Y}}$ . Fitting this form to our results we find  $\lambda_r \approx 3.1$  for Eq. (3.11), and  $\lambda_r \approx 2.9$  for Eq. (5.1). The normalization factor  $Q_0$  is found to be a factor 1.6 higher for (3.11) than for (5.1). For BFKL without the kinematical constraint we again find  $\lambda_r \approx 2.9$ .

Figure 19 shows the comparison between the two versions of the CCFM evolution, Eqs. (3.11) and (3.12), in the linear case (no saturation boundary) and for a running coupling. We see that (3.12) gives a faster growth, but the shapes of the curves are similar; this was to be expected in view of the discussion in Sect. 4.2. The corresponding results after adding the saturation boundary are shown in Fig. 20. It is then find that the speeds of the saturation fronts are quite similar, with Eq. (3.12) giving a slightly larger speed, meaning a higher value for the saturation exponent. Up to the  $Y$  values shown in

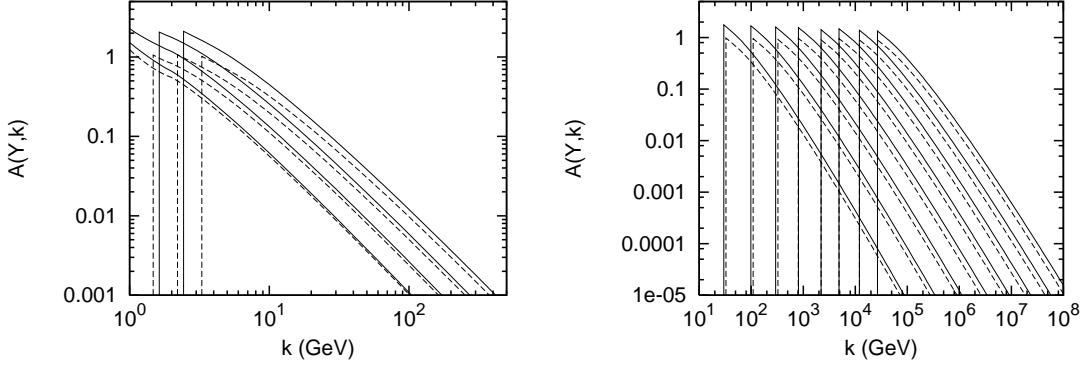


Figure 21: Comparing the solutions to Eq. (3.11) (with saturation boundary and running coupling) using two set of values for the saturation parameters:  $c = 0.1, \Delta = 5.0$  (solid lines),  $c = 0.4, \Delta = 2.0$  (dashed lines). Left:  $Y = 8, 10, 12, 14$ . Right:  $Y$  between 30 and 100.

the figure, we find the value  $\lambda_r \approx 3.3$  for (3.12) compared to the value  $\lambda_r \approx 3.1$  for (3.11) mentioned before. The difference in the normalization factor  $Q_0$  is a factor 1.4, with (3.12) giving the larger value.

So far all these results have been obtained for the fixed set of values  $c = 0.1$  and  $\Delta = 5.0$ . Theoretically, the different values of  $c$  and  $\Delta$  should only affect the absolute normalization of the gluon distribution and of  $Q_s$ , while leaving unchanged their shape and, respectively, energy dependence. To check these expectations and illustrate the robustness of our results we now repeat some of the calculations with the set  $c = 0.4$  and  $\Delta = 2.0$ . (Recall that these two parameters are correlated as  $\Delta \sim \ln 1/c$ .)

In Fig. 21 we compare the results obtained with the two sets of values for the case of Eq. (3.11). For the phenomenologically relevant values between  $Y = 8$  and 14, it appears that the curves are moving with slightly different speeds, and it seems that there is a slight difference in the slope of the gluon distribution which cannot be removed by a pure rescaling. The differences are, however, tiny and are not significant within the numerical certainty. For a much larger interval  $Y$  where the differences should become more visible, we in fact see that the shapes of the curves and their speed are very similar to each other. The difference in normalization is around a factor 1.5, with the solutions with  $c = 0.4$  and  $\Delta = 2.0$  lying below the default ones. Furthermore, in Fig. 22 we show a comparison between Eqs. (3.11) and (5.1) using this new set of parameters. We have here again scaled up the solutions to (5.1), but this time by a factor of 5.5, compared to 6.5 in Fig. 18. Once again, the two sets of fronts appear to have similar speeds and shapes, with the CCFM solution progressing slightly faster than the BFKL one. We have checked that the speeds of the fronts come out the same as in the default case of Fig. 18.

Let us finally consider different versions of the saturation boundary, to see whether this might affect our results. So far we have always applied a totally absorptive boundary to mimic the non-linear physics of saturation. From a theoretical viewpoint, it should be no fundamental difference between enforcing  $\mathcal{A}$  to vanish behind the saturation front, or fixing it to some non-zero constant value of order one: various choices for this value must

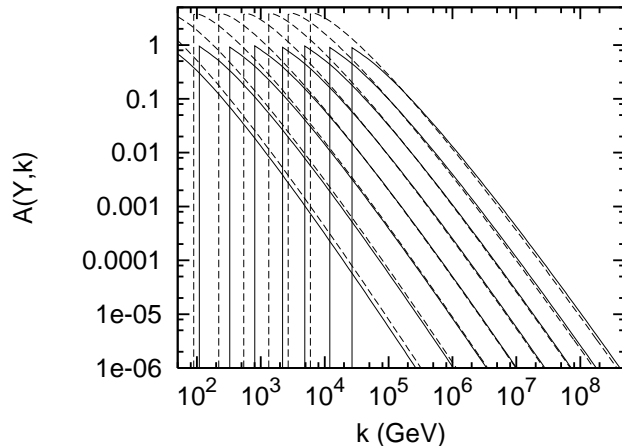


Figure 22: Comparing the solutions of Eqs. (3.11) and (5.1) for  $c = 0.4$ ,  $\Delta = 2.0$ , and large  $Y$  between 30 and 100 units. The solutions to (5.1) have been scaled up by a factor 5.5.

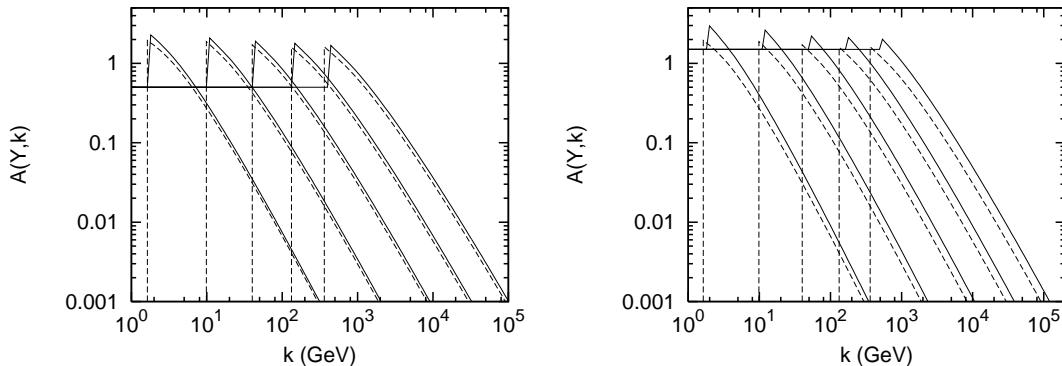


Figure 23: The solutions to Eq. (3.11) with different boundary conditions for a running  $\bar{\alpha}_s$ , and for  $Y = 10, 20, 30, 40$  and  $50$ . Left:  $\mathcal{A} = 0.5$  (solid lines) compared to the default  $\mathcal{A} = 0$  (dashed lines). Right:  $\mathcal{A} = 1.5$  (solid lines) compared to the default  $\mathcal{A} = 0$  (dashed lines).

lead to the same front dynamics at asymptotically high energies. One may however wonder whether differences can be important in practice, for non asymptotic energies. We have therefore tried two other boundary conditions as well, namely  $\mathcal{A} = 0.5$  and respectively  $\mathcal{A} = 1.5$ . The corresponding results are shown in Fig. 23, where they are also compared to the results obtained with the absorptive boundary condition  $\mathcal{A} = 0$ . The differences are found to be rather minor and correspond more or less to rescaling the gluon distribution. In particular, the energy dependence of  $Q_s$  and the shape of  $\mathcal{A}$  come out the same in all cases and for values of  $Y$ , including the relatively small ones.

## Acknowledgements

We would like to thank Gösta Gustafson and Gavin Salam for valuable discussions. This work is supported in part by Agence Nationale de la Recherche via the programme

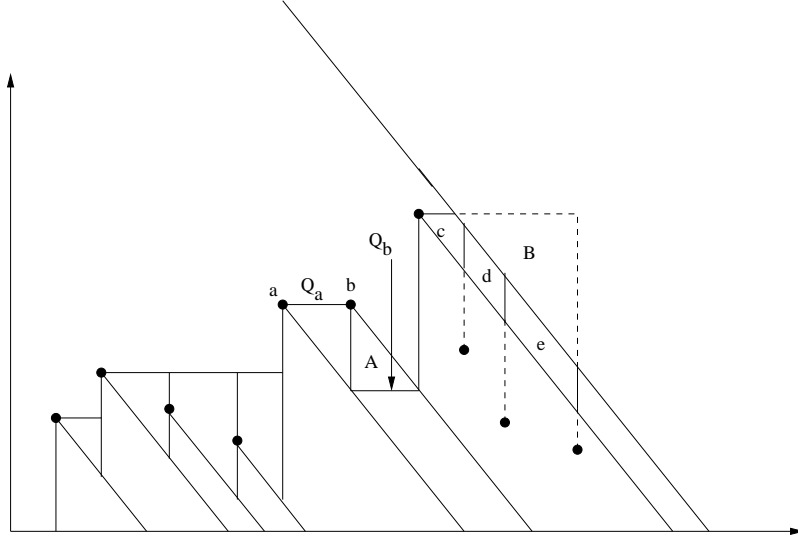


Figure 24: The representation of the situation where the real gluon (gluon  $b$ ) takes a large fraction of the transverse momentum of the virtual propagator emitting it ( $Q_a$ ). The next propagator  $Q_b$  satisfies  $Q_b < q_b$ . In this case the correct non-Sudakov is obtained by integrating over region  $A$  with opposite sign.

ANR-06-BLAN-0285-01.

### A. On the correct form of $\Delta_{ns}$

In this appendix we would like to make clear the correct form of the non-Sudakov form factor  $\Delta_{ns}$ , as it is usually written in a way which is not entirely correct. In the literature one usually finds the formula

$$\begin{aligned} \Delta_{ns}(k) &= \exp\left(-\bar{\alpha}_s \int_{z_k}^1 \frac{dz}{z} \int \frac{dq^2}{q^2} \theta(Q_k^2 - q^2) \theta(q^2 - z^2 p_k^2)\right) \\ &= \exp\left(-\bar{\alpha}_s \ln\left(\frac{z_0}{z_k}\right) \ln\left(\frac{Q_k^2}{z_0 z_k p_k^2}\right)\right), \end{aligned} \quad (\text{A.1})$$

where

$$z_0 = \begin{cases} 1 & \text{if } Q_k/p_k > 1 \\ Q_k/p_k & \text{if } z_k < Q_k/p_k \leq 1 \\ z_k & \text{if } Q_k/p_k \leq z_k \end{cases}$$

In this formula, the integrand is always negative so that  $\Delta_{ns}$  always gives a suppression. Although this seems reasonable, it is, however, not correct.

When we identified the areas  $A_k$  in Fig. 7 we assumed  $Q_k > z_k q_k$ . Consider now the set of emissions in Fig. 24. Here we also show the maximum allowed angle  $\bar{\xi}$ . Note that the region  $B$  would have been included in BFKL but is excluded in CCFM. The smaller regions  $c$ ,  $d$  and  $e$  are included in CCFM. The interesting region here is the one marked by  $A$ . It is contained within the region  $C_b$  and therefore also in the Sudakov associated

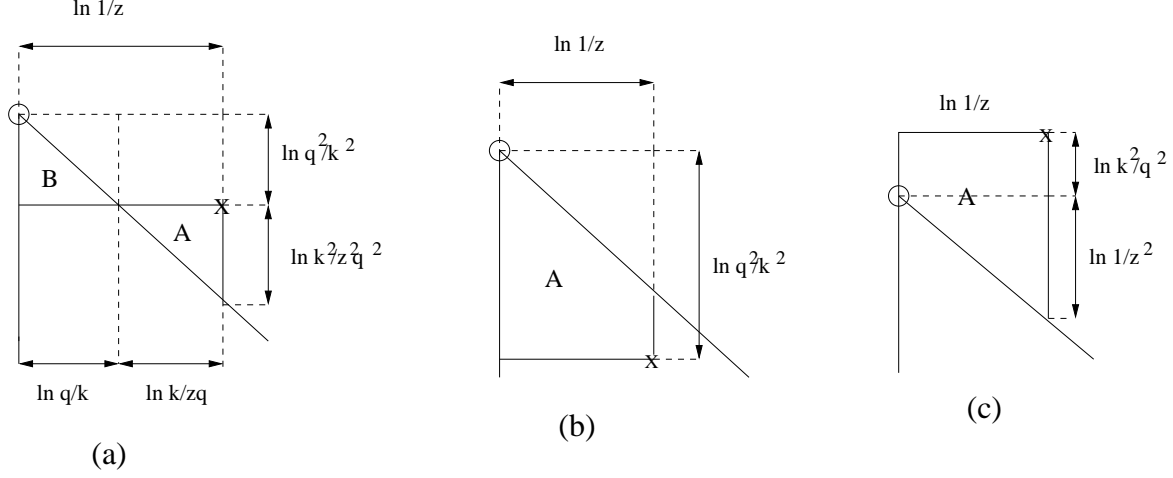


Figure 25: Closer inspection of the phase region over which the non-Sudakov is integrated. The correct result is obtained by subtracting the regions  $B$  (in figure (a)) and  $A$  (in figure (b)). The results are given in the text.

with the gluon  $b$ . When  $b$  is emitted from  $Q_a$ , it takes almost all transverse momentum so that  $Q_a \approx q_b \gg Q_b$ . The region  $A$  is thus bounded from below by  $Q_b$  as shown in the figure. Here indeed  $z_b q_b > Q_b$ , and if we set  $\Delta_{ne} = 1$  here so that it does not contribute then we have only the contribution from the Sudakov form factor in this region. However, there should actually be no net contribution from the form factors in this region. To see this one should remember the result in Fig. 3; when we multiply  $S_{ne}$  and  $S_{eik}$ , what is left over is a region bounded from above by the virtual propagators  $Q_k$ .

There should therefore be no net contribution from the form factors in region  $A$ . Thus in this region the Sudakov and the non-Sudakov must cancel each other. If this is to happen we have to set

$$\Delta_{ne} = \exp(+\bar{\alpha}_s A) \quad (\text{A.2})$$

here and not  $\Delta_{ne} = 1$ .

Actually let us from geometrical considerations derive the formula for  $\Delta_{ns}$  more carefully. In Fig. 25 we show the phase space over which the non-Sudakov is integrated. In figure (a) we have (denoting the virtual gluon momentum by  $k$  and the real gluon momentum by  $q$ )

$$\Delta_{ns} = \exp(-\bar{\alpha}_s (B - A)) \quad (\text{A.3})$$

where the areas  $A$  and  $B$  are marked in the figure. We see that

$$B - A = \ln^2 \frac{k}{zq} - \ln^2 \frac{k}{q} = \ln \frac{1}{z} \ln \frac{k^2}{zq^2}. \quad (\text{A.4})$$

For figure  $b$  we instead have

$$\Delta_{ns} = \exp(-\bar{\alpha}_s (-A)), \quad (\text{A.5})$$

and

$$A = \ln \frac{1}{z} \ln \frac{q^2}{k^2} - \ln^2 \frac{1}{z} = -\ln \frac{1}{z} \ln \frac{k^2}{zq^2}, \quad (\text{A.6})$$

while for figure (c) we have

$$\Delta_{ns} = \exp(-\bar{\alpha}_s A), \quad (\text{A.7})$$

and

$$A = \ln \frac{1}{z} \ln \frac{k^2}{q^2} + \ln^2 \frac{1}{z} = \ln \frac{1}{z} \ln \frac{k^2}{zq^2}. \quad (\text{A.8})$$

Thus  $\Delta_{ns}$  is indeed given by the formula in (2.21). As remarked before we see that  $\Delta_{ns}$  always gives a suppression if  $k^2 > zq^2$ , that is if the kinematical constraint is assumed to hold.

## B. Non leading effects in the CCFM equation

When deriving the formulas for  $\Delta_{ns}$  and  $\Delta_s$  in (2.21) and (2.23) from the original form factors in (2.3) and (2.4), recoils were not taken into effect. In this section we will propose modifications to (2.21) and (2.23) in order to more properly take into account recoil effects. Although such effects are formally suppressed, experience tells us that they can be quite important for phenomenology. For example in reference [46],  $\Delta_{ns}$  was modified beyond the leading order in a simple way, and it turns out that the modification is significant for phenomenology. Besides, in the Monte Carlo implementation in CASCADE full energy-momentum conservation is already taken into account and one has then no reason not to modify the virtual form factors accordingly.

For the sake of demonstration we will distinguish between the momenta of the  $t$ -channel gluons in the angular and, respectively, energy ordered cascades, that we shall denote as  $K_i$  and, respectively,  $Q_i$ . (Recall that  $K_i$  and  $Q_i$  differ by soft gluon effects which have been neglected in the main text.) In Fig. 26 we again show a gluon chain, but this time including the recoils that were so far neglected. The shaded areas here show the difference in phase space between the original expressions in (2.3) and (2.4), and  $\Delta_{ns}$  and  $\Delta_s$ . The horizontal dashed lines in the figure represent  $Q_i$  while the  $K_i$  are marked by crosses as before. So actually also the region between the dashed horizontal lines and the solid lines represent the differences although we have not shaded them. The problem is that it is difficult to take into account this difference since we cannot construct the exact  $Q_i$  until the whole chain has been generated, as the final energy ordering is a priori not known. We will, however, see how we can take into account the shaded regions by modifying  $\Delta_{ns}$  and  $\Delta_s$ .

What we see is that one generally overestimates the phase region included in  $\Delta_{ns}$  and  $\Delta_s$ . This means that one overestimates the suppression coming from these factors. Actually in some of the shaded regions in the figure both  $\Delta_{ns}$  and  $\Delta_s$  overestimate the phase region so we get double extra suppression. Let us first concentrate on the soft emissions. For the soft emission  $p_i$ , the  $y$  integral is integrated up to  $x_{i-1}$ . Now this will always cause an overestimate since the subsequent emissions are emitted from  $K_i$  with energy  $x_i < x_{i-1}$ , and when eventually the next hard gluon is emitted it will have energy



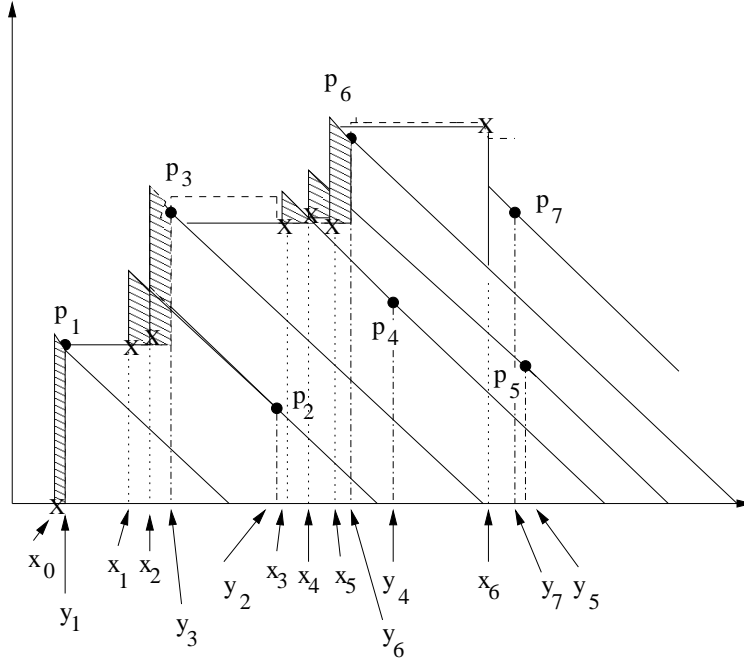


Figure 26: A CCFM chain in the phase space, including also recoils in the emissions. The shaded regions indicate the difference in phase space between the original expression in (2.3) and (2.4), and the form factors  $\Delta_{ns}$  and  $\Delta_s$ .

less than  $x_i$  itself. Thus we see that it would be better to have the energy integral in  $\Delta_s$  for the soft emission integrated up to  $x_i$ , instead of  $x_{i-1}$ . Ideally we would like to have had the integral up to the energy of the next hard gluon, but of course we do not know what that energy will be beforehand. Thus we propose that

$$\Delta_s^{soft}(i) \rightarrow \exp \left( -\bar{\alpha}_s \int_{\xi_{i-1}}^{\xi_i} \frac{d\xi}{\xi} \int_{\epsilon}^{x_i} \frac{dy}{y} \right) \quad (\text{B.1})$$

for soft emissions. Again writing this in terms of momenta we get

$$\Delta_s^{soft}(k) = \exp \left( -\bar{\alpha}_s \int_{z_{k-1}^2 p_{k-1}^2}^{p_k^2} \frac{dp^2}{p^2} \int_{\epsilon'}^{z_i} \frac{dy}{y} \right). \quad (\text{B.2})$$

which should be compared to (2.23) (again  $\epsilon' = q_0/p$ ). We see that the difference in the  $y$  integral is

$$\int_{\epsilon'}^1 \frac{dy}{y} - \int_{\epsilon'}^{z_i} \frac{dy}{y} = \ln \frac{1}{z_i} \quad (\text{B.3})$$

where of course for soft emissions  $z_i \approx 1$ .

However, now we can also see that there is a region between  $x_{i-1}$  and  $x_i$  which is missed since the contribution from  $\Delta_s^{soft}$  has been removed from this region, as illustrated

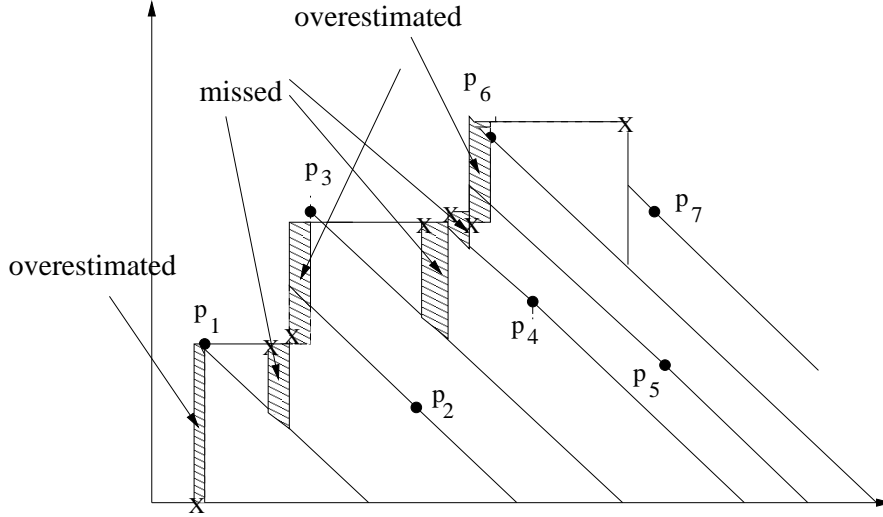


Figure 27: The shaded regions marked “missed” are regions which contribute to the original form factors but not to the new form factors, after the Sudakov for the soft emissions has been modified. Regions marked “overestimated” are regions where we have too much suppression due to the new form factors. These differences can be removed by modifying the non-Sudakov and Sudakov form factors.

in Fig. 27. Of course by removing that contribution we get rid of the potentially large overestimate of the phase region. The missing parts would have had zero area if there were no recoils, since then  $x_{i-1}$  and  $x_i$  would have been equal. Thus we can fill in this region by associating a non-Sudakov  $\Delta_{ns}^{soft}$  with the soft emissions as well. It is easy to see from Fig. 27 that the missed part extends down from  $K_{i-1}$  to the angle of emission  $i-1$ , *i.e.* to  $\xi_{i-1}$ . Thus for each soft emission we associate

$$\Delta_{ns}^{soft}(i) = \exp \left( -\bar{\alpha}_s \int_{z_i}^1 \frac{dz}{z} \int_{z^2 p_{i-1}^2}^{K_{i-1}^2} \frac{dp^2}{p^2} \right) \quad (\text{B.4})$$

which we have written in terms of the rescaled momenta as before. Again if  $K_{i-1} < z p_{i-1}$ , (B.4) will give an enhancement in some region but this is correct since in that case it will cancel an oversuppression coming from  $\Delta_s$ .

From Fig. 27 we can see that there are still some regions in which we have an oversuppression coming from both  $\Delta_s$  and from  $\Delta_{ns}$  associated with the hard emissions. Actually depending on the kinematics (when  $K_i < z_i p_i$ ),  $\Delta_{ns}$  will cancel the oversuppression from  $\Delta_s$  in some small region. This has been taken into account in Fig. 27. As one can see one overestimates the phase region when  $q_i > K_{i-1}$ . Therefore in this case we can modify the

form factors as follows

$$\begin{aligned}\Delta_s^{hard}(i) &\rightarrow \exp\left(-\bar{\alpha}_s \int_{\xi_{i-1}}^{\xi_i} \frac{d\xi}{\xi} \int_{\epsilon}^{y_i} \frac{dy}{y}\right) \quad \text{if } q_i > K_{i-1} \\ &= \exp\left(-\bar{\alpha}_s \int_{z_{i-1}^2 p_{i-1}^2}^{p_i^2} \frac{dp^2}{p^2} \int_{\epsilon'}^{1-z_i} \frac{dy}{y}\right)\end{aligned}\quad (\text{B.5})$$

$$\begin{aligned}\Delta_{ns}^{hard}(i) &\rightarrow \exp\left(-\bar{\alpha}_s \int_{x_i}^{y_i} \frac{dy}{y} \int_{\xi_i}^{\xi(K_i^2)} \frac{d\xi}{\xi}\right) \quad \text{if } q_i > K_{i-1} \\ &= \exp\left(-\bar{\alpha}_s \int_{\frac{z_i}{1-z_i}}^1 \frac{dz}{z} \int_{z^2 p_i^2}^{K_i^2} \frac{dq^2}{q^2}\right)\end{aligned}\quad (\text{B.6})$$

so that in each factor we integrate in energy up to  $y_i$  instead of integrating up to  $x_{i-1}$ . In this way we minimize the overestimation of the true phase region.

To summarize, the standard splitting probability for the emission of the  $i$ th gluon which is given by

$$dP(i) = \bar{\alpha}_s dz_i \frac{d^2 p_i}{\pi p_i^2} \left( \frac{\Delta_{ns}(i)}{z_i} + \frac{1}{1-z_i} \right) \Delta_s(i) \theta(p_i - z_{i-1} p_{i-1}) \quad (\text{B.7})$$

with  $\Delta_s(i)$  given in (2.23) and  $\Delta_{ns}(i)$  in (2.21), is now replaced by

$$\begin{aligned}dP(i) &= \bar{\alpha}_s dz_i \frac{d^2 p_i}{\pi p_i^2} \left( \theta(K_{i-1} - (1-z_i)p_i) \left( \frac{\Delta_{ns}(i)\Delta_s(i)}{z_i} + \frac{\Delta_{ns}^{soft}(i)\Delta_s^{soft}(i)}{1-z_i} \right) + \right. \\ &\quad \left. \theta((1-z_i)p_i - K_{i-1}) \left( \frac{\Delta_{ns}^{hard}(i)\Delta_s^{hard}(i)}{z_i} + \frac{\Delta_{ns}^{soft}(i)\Delta_s^{soft}(i)}{1-z_i} \right) \right) \theta(p_i - z_{i-1} p_{i-1})\end{aligned}\quad (\text{B.8})$$

where  $\Delta_s^{soft}(i)$ ,  $\Delta_{ns}^{soft}(i)$ ,  $\Delta_s^{hard}(i)$  and  $\Delta_{ns}^{hard}(i)$  are given by (B.2), (B.4), (B.5) and (B.6) respectively.

It is really non-trivial to implement these changes in the type of numerical procedure that we use in this paper. However, they are suitable for implementing in a Monte Carlo procedure and as such it would be straightforward to implement them in CASCADE, and it would be interesting to see how large the effects are. One can also put in theta functions to make sure that for example  $z < 0.5$  for hard emissions, and  $z > 0.5$  for soft emissions.

### C. Rewriting $\Delta_{ns}$ in CCFM and the comparison to BFKL

In the literature one usually finds the statement that Eq. (3.2) reduces to the BFKL equation in the high energy limit. In this appendix we would like to elaborate more on this. The key point to this statement is the derivation of  $\Delta_{ns}$  appropriate in the formal high energy limit, where energy is infinite, and importantly  $\bar{\alpha}_s \rightarrow 0$  for *fixed*  $q_0$ .

Previously we derived  $\Delta_{ns}$  following figure 25. In this case, however, we must consider what happens in case  $z$  is so small that the diagonal line through  $q$ , on which  $\xi$  is constant

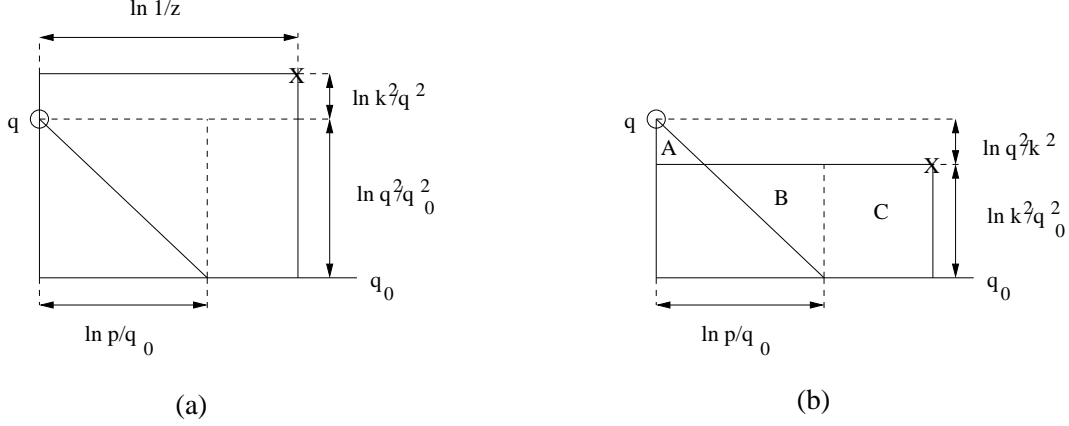


Figure 28: The phase space for  $\Delta_{ns}$  in CCFM in case we take very large steps in  $z$ , such that  $z < q_0/p$ .

and equal to the angle of the real gluon  $q$ , cuts the line representing the soft cutoff  $q_0$  before cutting the vertical line through  $k$ . This situation is illustrated in Fig. 28. The horizontal line at the bottom just indicates the momentum cut  $q_0$ . What happens here is that  $z < q_0/p$  where  $p$  is the rescaled momentum of the real emitted gluon  $q$ . Actually since we now consider the small  $z$  limit, there is no need to make a distinction between the rescaled and the regular momenta, thus one might as well set  $p = q$ . From figure (a), one can see that  $\Delta_{ns}$  is integrated over a region of total size

$$\begin{aligned}
 A &= \ln \frac{q^2}{q_0^2} \cdot \left( \ln \frac{1}{z} - \frac{1}{2} \ln \frac{p}{q_0} \right) + \ln \frac{k^2}{q^2} \ln \frac{1}{z} \\
 &= \ln \frac{1}{z} \ln \frac{k^2}{q_0^2} - \ln^2 \frac{q}{q_0}
 \end{aligned} \tag{C.1}$$

where in the last equality we have just set  $p = q$ .  $\Delta_{ns}$  is then given by  $\exp(-\bar{\alpha}_s A)$ . In the case shown in figure (b) we instead have

$$\Delta_{ns} = \exp(-\bar{\alpha}_s(-A + B + C)), \tag{C.2}$$

where

$$\begin{aligned}
 -A + B + C &= \ln \frac{1}{z} \ln \frac{k^2}{q_0^2} + \ln \frac{p}{q_0} \ln \frac{k^2}{pq_0} - \ln \frac{p}{q_0} \ln \frac{k^2}{q_0^2} \\
 &= \ln \frac{1}{z} \ln \frac{k^2}{q_0^2} - \ln^2 \frac{q}{q_0}
 \end{aligned} \tag{C.3}$$

where we have again set  $p = q$  in the last equality. We now remember that the virtual form factor is in BFKL given by (2.6), which equals

$$\exp \left( -\bar{\alpha}_s \ln \frac{1}{z} \ln \frac{k^2}{q_0^2} \right). \tag{C.4}$$

Assuming now that the typical  $z$  are so small that the result in (C.1) is valid, we can write the CCFM non-Sudakov form factor as

$$\Delta_{ns}(z, k, q) = \Delta(z, k) \cdot \Delta^R(q) \quad (\text{C.5})$$

where  $\Delta(z, k)$  is the BFKL form factor, and

$$\Delta^R(q) = \exp\left(\bar{\alpha}_s \ln^2 \frac{q}{q_0}\right) \quad (\text{C.6})$$

with the "R" standing for "Residual". In this case Eq. (3.2) can be written as

$$\mathcal{A}(Y, k, \bar{q}) = \bar{\alpha}_s \int_0^Y dy \int \frac{d^2 q}{\pi q^2} \theta(Y - y + \ln(\bar{q}/q)) \Delta(Y - y, k) \Delta^R(q) \mathcal{A}(y, k', q), \quad (\text{C.7})$$

where  $\Delta$  is the BFKL non-Sudakov form factor, while  $\Delta^R(q)$  is given in (C.6) and is independent of  $Y$ . Now of course if one considers the leading contributions in  $Y - y$ , then the angular ordering theta function can be neglected and, since we moreover have  $\bar{\alpha}_s \rightarrow 0$  one can let  $\Delta^R \rightarrow 1$ . In that case obviously the BFKL equation is recovered.

It is obvious from the derivation here that the form for  $\Delta_{ns}$  is appropriate only for very high energies, and for  $\bar{\alpha}_s \rightarrow 0$  with fixed cutoff  $q_0$ . Thus if one makes a certain calculation, for example jet production rates using  $q_0$  as a resolution scale, one needs to be careful considering the limit when  $q_0 \rightarrow 0$ . Obviously in that case we gradually go from the situation in Fig. 28 to the situation in Fig. 25. This means that we go from the result (C.1) to the result in (2.21), in which case the similarity to BFKL is somewhat lost. For similar discussions see also [38, 47, 39]. Of course in a sense this is a bit artificial since from the beginning we had that  $S_{ne}^2 \cdot S_{cik}^2 = \Delta^{BFKL}$ , but remember also the discussion at the end of section 2.3.

#### D. Increasing the accuracy of the real-virtual cancellations

In this final appendix, we would like to discuss a bit more carefully the definition of the  $k_\perp$ -conserving emissions, and the real-virtual cancellations discussed in section 3. We were not very careful when defining the  $k_\perp$ -conserving emissions, and especially the situation when the momenta of these emissions,  $q$ , become comparable to  $k$  was not discussed. To be more careful, one would have liked to define  $k_\perp$ -conserving emissions as emissions with say  $q < ak$  for some  $a$  which is strictly smaller than 1, as this would give a better accuracy. As the procedure in section 3 gives rise to an intercept higher than BFKL, one might try to thus increase the accuracy in the definition of the  $k_\perp$ -conserving emissions to derive a new equation. Indeed we saw in section 4.2 that a better agreement with BFKL was obtained in the asymptotic limit if a constant negative term proportional to the gluon distribution is added to the equation. As such a contribution is related to the virtual corrections, we might indeed guess that it has something to do with the real-virtual cancellations.

The issue of improving the accuracy in the definition of the  $k_\perp$ -conserving emissions was discussed first in [38], again considering only the possibility that  $k > k'$ . In our case

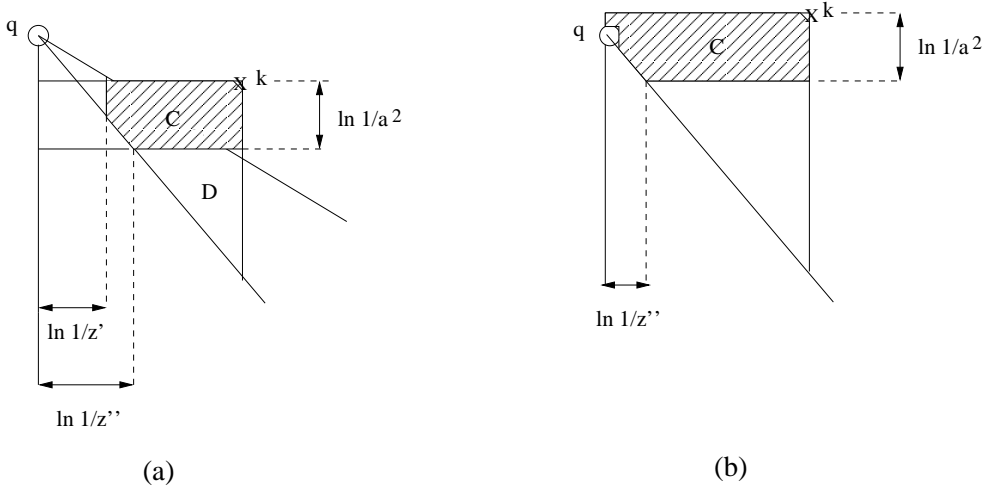


Figure 29: (a): Region  $D$  is the region where we have real  $k_{\perp}$ -conserving emissions when the accuracy of the definition of  $k_{\perp}$ -conserving emissions are improved. The shaded region is than the region left over by the real-virtual cancellation. Here  $q > k$ . It is seen that  $z' = k^2/q^2$  and  $z'' = ak/q$ . We have assumed  $z' > z''$ , and the case  $z' < z''$  is discussed in the text. (b): Same as in figure (a) but now for  $q < k$ .

we also look at the opposite case, again with the kinematical constraint included. The procedure is the same as before, and one can easily derive new evolution equations. As we later discuss, however, this procedure does not simplify the problem of solving the more exclusive equation in (3.2), although it sheds some light on the physical origin of the discrepancy between BFKL and the asymptotic behaviour of equations (3.11) and (3.12).

Since now the  $k_{\perp}$ -conserving emissions have momenta  $a$  times smaller than the corresponding virtual propagator, they will not completely cancel  $\Delta_{ns}$ , but there will be a region left over from the cancellation. Assume first that  $k < q$ . Remember from Fig. 9 that  $\Delta_{ns} = \exp(-\bar{\alpha}_s A)$  where  $A$  was defined in the figure. The region  $A$  from Fig. 9 is then the sum of the regions  $C$  and  $D$  in Fig. 29(a),  $A = C + D$ . Region  $D$  is the region where we have the real  $k_{\perp}$ -conserving emissions, and summing over these emissions we get a factor  $\exp(\bar{\alpha}_s D)$  and what is left from the multiplication with  $\Delta_{ns}$  is therefore  $\exp(-\bar{\alpha}_s C)$ . From Fig. 29(a) we see that

$$\begin{aligned}
 C &= \ln \frac{1}{a^2} \ln \frac{z'}{z} - \frac{1}{2} \ln \frac{z'^2 q^2}{a^2 k^2} \ln \frac{z'}{z''} \\
 &= \ln \frac{1}{a^2} \ln \frac{k^2}{z q^2} - \ln^2 \frac{k}{a q} = \ln \frac{1}{z} \ln \frac{1}{a^2} - \ln^2 \frac{q}{a k}.
 \end{aligned} \tag{D.1}$$

If instead  $k > q > ak$ , we see from Fig. 29(b) that region  $C$  is again given by the formula above. Thus this is the region left over by the cancellations. Actually, in Fig. 29(a) we assumed that  $z' > z''$  which means that  $a < k/q$ . If instead  $a > k/q$  we get a slightly different situation, since the region  $C$  would then be replaced by a rectangular region. In that case it is easy to see that we get

$$C' = \ln \frac{1}{a^2} \ln \frac{k^2}{z q^2} = \ln \frac{1}{z} \ln \frac{1}{a^2} - \ln^2 \frac{q}{a k} + \ln^2 \frac{k}{a q} \tag{D.2}$$

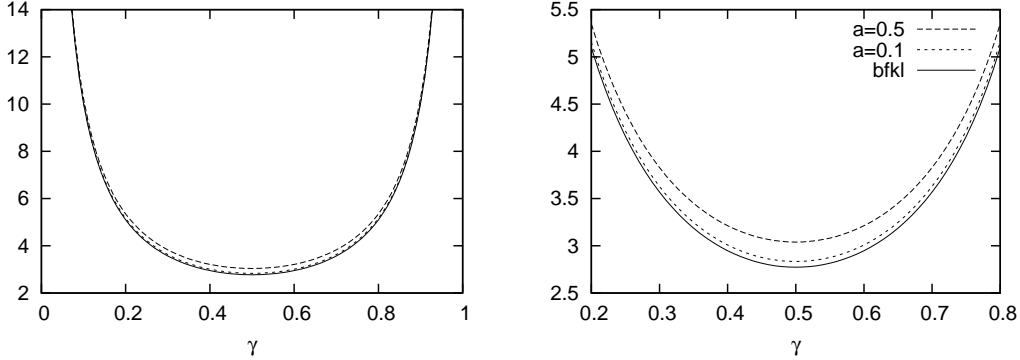


Figure 30: The Mellin space eigenfunction of Eq. (D.4) for  $a = 0.5$  (long dashed lines) and  $a = 0.1$  (short dashed lines) for  $\bar{\alpha}_s \rightarrow 0$  together with the BFKL eigenfunction (solid lines).

which contains an extra term compared to the formula for  $C$ . Since in this case  $k < q$ , we can neglect the last term, however. Actually we could well approximate the regions  $C$  and  $C'$  by the first term only (which contains  $\ln(1/z)$ ). This is indeed appropriate as we will below only study the asymptotic limit. We see that this term will generate an additional contribution in the right-hand side of the differential equation which reads

$$- \bar{\alpha}_s \ln \frac{1}{a^2} \mathcal{A}(Y, k). \quad (\text{D.3})$$

This is infact the term we were looking for in order to reduce the Mellin space eigenfunction. However, note also that we have real emissions left over in the same region and these will modify the real kernel as well. We will write down the asymptotic equation below and study its Mellin transform.

Before doing that, let us comment on the procedure of generating new equations. As an explicit constraint we can obviously use  $q > \min(ak, ak')$ . The problem now, however, is that we can no longer justify the step from (3.7) to (3.8) where we dropped all the dependence on the third parameter in the argument of  $\mathcal{A}$ . The dependence on  $\bar{q}$  drops again on account of the kinematical constraint, but we can no longer guarantee that  $q \geq k'$ . If we nevertheless assume this then we lose the accuracy gained by introducing  $a$ . Infact if it was possible to drop all dependence on the third parameter by just using the kinematical constraint, then we would not need to bother cancelling  $\Delta_{ns}$  since it would have been equally easy to solve (3.2) directly. As far as the asymptotic behaviour is concerned, however, we are justified to go from (3.7) to (3.8). (Unless we are looking at the  $\bar{\alpha}_s \rightarrow 0$  limit, we would not be able to drop the second and third terms in (D.1) and (D.2) anyway.) Thus to study the intercept we make the same steps as before and arrive at the asymptotic equation

$$\partial_Y \mathcal{A}(Y, k) = \bar{\alpha}_s \int \frac{dk'^2}{|k^2 - k'^2|} h_a(\kappa) \mathcal{A}(Y, k') - \bar{\alpha}_s \ln \frac{1}{a^2} \mathcal{A}(Y, k), \quad (\text{D.4})$$

where now

$$h_a(\kappa) = 1 - \frac{2}{\pi} \arctan \left( \frac{1 + \sqrt{\kappa}}{1 - \sqrt{\kappa}} \sqrt{\frac{2\sqrt{\kappa} - 1 - (1 - a^2)\kappa}{2\sqrt{\kappa} + 1 + (1 - a^2)\kappa}} \right) \theta(2\sqrt{\kappa} - (1 - a^2)\kappa - 1), \quad (\text{D.5})$$

and  $\kappa$  is defined as before.

It is straightforward to study the Mellin space eigenfunction numerically. In Fig. 30 we plot the eigenfunction for  $a = 0.5$  and  $a = 0.1$  together with the BFKL result. As  $a$  decreases we indeed see that the curves move toward the BFKL eigenfunction. We basically get a constant shift around  $\gamma = 0.5$ , and the behaviour at the endpoints  $\gamma = 0, 1$  is not changed. For the intercept, one goes from 3.23 at  $a = 1$  to 3.02 at  $a = 0.5$ , and 2.83 at  $a = 0.1$ . The saddle point occurs at  $\gamma = 0.5$  in all cases. The saturation saddle point moves from  $\gamma_s \approx 0.35$  at  $a = 1$  towards  $\gamma_s \approx 0.37$  at  $a = 0.1$ .

## References

- [1] E. Avsar and E. Iancu *Phys. Lett.* **B673** (2009) 24–29, 0901.2873.
- [2] L.N. Lipatov, *Sov. J. Nucl. Phys.* **23** (1976) 338;  
E.A. Kuraev, L.N. Lipatov and V.S. Fadin, *Zh. Eksp. Teor. Fiz* **72**, 3 (1977) (*Sov. Phys. JETP* **45** (1977) 199);  
Ya.Ya. Balitsky and L.N. Lipatov, *Sov. J. Nucl. Phys.* **28** (1978) 822.
- [3] M. Ciafaloni *Nucl. Phys.* **B296** (1988) 49.
- [4] S. Catani, F. Fiorani, and G. Marchesini *Nucl. Phys.* **B336** (1990) 18.
- [5] S. Catani, F. Fiorani, and G. Marchesini *Phys. Lett.* **B234** (1990) 339.
- [6] E. Iancu, K. Itakura, and L. McLerran *Nucl. Phys.* **A708** (2002) 327–352, hep-ph/0203137.
- [7] A. H. Mueller and D. N. Triantafyllopoulos *Nucl. Phys.* **B640** (2002) 331–350, hep-ph/0205167.
- [8] S. Munier and R. Peschanski *Phys. Rev. Lett.* **91** (2003) 232001, hep-ph/0309177.
- [9] E. Iancu, A. H. Mueller, and S. Munier *Phys. Lett.* **B606** (2005) 342–350, hep-ph/0410018.
- [10] A. Dumitru, E. Iancu, L. Portugal, G. Soyez, and D. N. Triantafyllopoulos *JHEP* **08** (2007) 062, arXiv:0706.2540 [hep-ph].
- [11] I. Balitsky *Nucl. Phys.* **B463** (1996) 99–160, hep-ph/9509348.
- [12] Y. V. Kovchegov *Phys. Rev.* **D60** (1999) 034008, hep-ph/9901281.
- [13] H. Jung and G. P. Salam *Eur. Phys. J.* **C19** (2001) 351–360, hep-ph/0012143.
- [14] H. Kharraziha and L. Lönnblad *JHEP* **03** (1998) 006, hep-ph/9709424.
- [15] D. N. Triantafyllopoulos *Nucl. Phys.* **B648** (2003) 293–316, hep-ph/0209121.
- [16] A. M. Stasto, K. Golec-Biernat, and J. Kwiecinski *Phys. Rev. Lett.* **86** (2001) 596–599, hep-ph/0007192.
- [17] E. Iancu, K. Itakura, and S. Munier *Phys. Lett.* **B590** (2004) 199–208, hep-ph/0310338.
- [18] G. Soyez *Phys. Lett.* **B655** (2007) 32–38, 0705.3672.
- [19] E. Iancu, M. S. Kugeratski, and D. N. Triantafyllopoulos *Nucl. Phys.* **A808** (2008) 95–116, 0802.0343.



- [20] CDF Collaboration, D. E. Acosta *et al.* *Phys. Rev.* **D70** (2004) 072002, hep-ex/0404004.
- [21] CDF Collaboration, R. D. Field hep-ph/0201192.
- [22] C. Marquet and L. Schoeffel *Phys. Lett.* **B639** (2006) 471–477, hep-ph/0606079.
- [23] F. Gelis, R. Peschanski, G. Soyez, and L. Schoeffel hep-ph/0610435.
- [24] V.N. Gribov and L.N. Lipatov, *Sov. Journ. Nucl. Phys.* **15** (1972), 438; G. Altarelli and G. Parisi, *Nucl. Phys.* **B126** (1977), 298; Yu. L. Dokshitzer, *Sov. Phys. JETP* **46** (1977), 641.
- [25] M. Klein and R. Yoshida *Prog. Part. Nucl. Phys.* **61** (2008) 343–393, 0805.3334.
- [26] S. Catani, M. Ciafaloni and F. Hautmann, *Nucl. Phys.* **B366** (1991), 135; S. Catani and F. Hautmann, *Nucl. Phys.* **B427** (1994), 475;.
- [27] J. Jalilian-Marian, A. Kovner, A. Leonidov and H. Weigert, *Nucl. Phys.* **B504** (1997) 415; *Phys. Rev.* **D59** (1999) 014014; J. Jalilian-Marian, A. Kovner and H. Weigert, *Phys. Rev.* **D59** (1999) 014015; A. Kovner, J. G. Milhano and H. Weigert, *Phys. Rev.* **D62** (2000) 114005.
- [28] E. Iancu, A. Leonidov and L. McLerran, *Nucl. Phys.* **A692** (2001) 583; *Phys. Lett.* **B510** (2001) 133; E. Ferreira, E. Iancu, A. Leonidov and L. McLerran, *Nucl. Phys.* **A703** (2002) 489; E. Iancu and L. McLerran, *Phys. Lett.* **B510** (2001) 145.
- [29] E. Iancu, *Color Glass Condensate and its relation to HERA physics*, arXiv:0901.0986 [hep-ph];  
A.H. Mueller, *Parton Saturation—An Overview*, hep-ph/0111244;  
E. Iancu, A. Leonidov and L. McLerran, *The Colour Glass Condensate: An Introduction*, hep-ph/0202270. Published in *QCD Perspectives on Hot and Dense Matter*, Eds. J.-P. Blaizot and E. Iancu, NATO Science Series, Kluwer, 2002;  
E. Iancu and R. Venugopalan, *The Color Glass Condensate and High Energy Scattering in QCD*, hep-ph/0303204. Published in *Quark-Gluon Plasma 3*, Eds. R.C. Hwa and X.-N. Wang, World Scientific, 2003;  
H. Weigert, *Evolution at small  $x_{\text{bj}}$ : The Color Glass Condensate*, *Prog. Part. Nucl. Phys.* **55** (2005) 461 [hep-ph/0501087].
- [30] B. Andersson, G. Gustafson, and J. Samuelsson *Nucl. Phys.* **B467** (1996) 443–478.
- [31] Small  $x$  Collaboration, B. Andersson *et al.* *Eur. Phys. J.* **C25** (2002) 77–101, hep-ph/0204115.
- [32] Small  $x$  Collaboration, J. R. Andersen *et al.* *Eur. Phys. J.* **C35** (2004) 67–98, hep-ph/0312333.
- [33] Small  $x$  Collaboration, J. R. Andersen *et al.* *Eur. Phys. J.* **C48** (2006) 53–105, hep-ph/0604189.
- [34] E. Avsar, G. Gustafson, and L. Lönnblad *JHEP* **07** (2005) 062, hep-ph/0503181.
- [35] E. Avsar, G. Gustafson, and L. Lönnblad *JHEP* **01** (2007) 012, hep-ph/0610157.
- [36] E. Avsar, G. Gustafson, and L. Lönnblad *JHEP* **12** (2007) 012, arXiv:0709.1368 [hep-ph].
- [37] C. Flensburg, G. Gustafson, and L. Lönnblad *Eur. Phys. J.* **C60** (2009) 233–247, 0807.0325.
- [38] G. P. Salam *JHEP* **03** (1999) 009, hep-ph/9902324.
- [39] G. Marchesini *Nucl. Phys.* **B445** (1995) 49–80, hep-ph/9412327.

- [40] J. Kwiecinski, A. D. Martin, and P. J. Sutton *Z. Phys.* **C71** (1996) 585–594, [hep-ph/9602320](#).
- [41] I. Balitsky *Phys. Rev.* **D75** (2007) 014001, [hep-ph/0609105](#).
- [42] Y. V. Kovchegov and H. Weigert *Nucl. Phys.* **A784** (2007) 188–226, [hep-ph/0609090](#).
- [43] I. Balitsky and G. A. Chirilli *Phys. Rev.* **D77** (2008) 014019, [arXiv:0710.4330](#) [[hep-ph](#)].
- [44] I. Balitsky and G. A. Chirilli [0903.5326](#).
- [45] W. Van Saarloos, *Phys. Rep.* **386** (2003) 29 [[arXiv:cond-mat/0308540](#)].
- [46] G. Bottazzi, G. Marchesini, G. P. Salam, and M. Scorletti *JHEP* **12** (1998) 011, [hep-ph/9810546](#).
- [47] J. R. Forshaw and A. Sabio Vera *Phys. Lett.* **B440** (1998) 141–150, [hep-ph/9806394](#).